RESEARCH ARTICLE

A Stable Poro-Mechanical Formulation for Material Point Methods Leveraging Overlapping Meshes and Multi-Field Ghost Penalisation

Giuliano Pretti [ID] | Robert E. Bird [ID] | Nathan D. Gavin | William M. Coombs [ID] | Charles E. Augarde

Department of Engineering, Durham University, Durham, UK

Correspondence: Charles E. Augarde (charles.augarde@durham.ac.uk)

ABSTRACT

The Material Point Method (MPM) is widely used to analyse coupled (solid-water) problems under large deformations/displacements. However, if not addressed carefully, MPM u-p formulations for poromechanics can be affected by two major sources of instability. Firstly, inf-sup condition violation can arise when the spaces for the displacement and pressure fields are not chosen correctly, resulting in an unstable pressure field when the equations are monolithically solved. Secondly, the intrinsic nature of particle-based discretisation makes the MPM an unfitted mesh-based method, which can affect the system's condition number and solvability, particularly when background mesh elements are poorly populated. This work proposes a solution to both problems. The inf-sup condition is avoided using two overlapping meshes, a coarser one for the pressure and a finer one for the displacement. This approach does not require stabilisation of the primary equations since it is stable by design and is particularly valuable for low-order shape functions. As for the system's poor condition number, a face ghost penalisation method is added to both the primary equations, which constitutes a novelty in the context of MPM mixed formulations. This study frequently makes use of the theories of functional analysis or the unfitted Finite Element Method (FEM). Although these theories may not directly apply to the MPM, they provide a robust and logical basis for the research. These rationales are further supported by four numerical examples, which encompass both elastic and elasto-plastic cases and drained and undrained conditions.

1 | Introduction

Since its initial publications [1, 2], the Material Point Method (MPM) has become a widely used method for modelling solid materials undergoing extreme deformations while maintaining a Lagrangian description of the equations. This versatility has been tested in several engineering applications, including snow avalanches [3, 4], ice dynamics [5, 6], slope stability [7, 8], soft robots [9], and biomedical applications [10], to name a few. However, the MPM has also been appreciated beyond its engineering purposes, especially in computer graphics simulations [11, 12].

Among the different applications, fields such as geotechnics and biomechanics deal with porous solid materials, whose mechanical behaviour is strongly influenced by the presence of an interstitial fluid. These materials are the subject of the study

of poromechanics [13]. MPM-based analyses investigating the behaviour of these materials have dramatically increased in the last few years, as the recent review papers by Zheng et al. [14] and Ceccato et al. [15] demonstrate. The choices available to run these studies are numerous, and they can be grouped into three main categories (see, in this regard, Soga et al. [16]), which depends on: (i) the selected primary variables; (ii) the number of sets of Material Points (MPs); and (iii) the temporal discretisation (explicit vs. implicit schemes).

The use of different primary equations, point (i), distinguishes between $u - p^{(f)}$, $v - w$, and $u - p^{(f)} - w$ formulations, where these formulations are labelled after the name of the primary unknowns (u or v is the displacement or velocity of the solid body, $p^{(f)}$ is the fluid pressure, and w the fluid velocity).

Since MPM formulations are based on a point-based discretisation (these are indeed the MPs), it is possible to choose how many sets of MPs can be employed in a poro-mechanical simulation (point (ii) of the above). In one case, one set of MPs can be considered, simultaneously keeping track of both phases of the mixed body. In the other, the solid and the fluid phases are separately represented by two sets of MPs. The best application of each combination of primary variables and the number of MP sets firmly depends upon the considered problem, and assessing these is beyond the scope of this work, which adopts a one-set $u - p^{(f)}$ formulation. The reader interested in a detailed explanation and classification of the above options can refer to these recent theses and references therein [17–19].

Point (iii) concerns the chosen temporal discretisation, which divides explicit from implicit formulations. On the one hand, explicit formulations (see, e.g., [20, 21]) are straightforward to implement, but their stable time-step selection is bounded (see [16]). Moreover, these schemes do not require updating of variables simultaneously and can, therefore, employ fractional-step (or staggered) schemes. Conversely, implicit schemes (see, e.g., [22]) are more computationally expensive and burdensome implementation-wise, but they can deal with larger time steps. These formulations employ monolithic solvers, where updated variables are computed at the same time. When close to nearly-undrained conditions, the system of equations solved in implicit formulations can suffer from the violation of *inf-sup* condition and exhibit oscillating pressure values. Alternatively, semi-implicit methods represent a hybridisation between explicit and implicit formulations. Generally speaking, these employ staggered schemes, where the displacement unknown is explicitly computed, while the pressure can be implicitly solved (see, for instance, the scheme used in a $u - p^{(f)} - v$ formulation by Kularathna et al. [23], or its extension to thermal problems studied by Yu et al. [24, 25]). However, depending on the predictor-corrector scheme, the use of a fractional-step technique might or might not suffer from the inf-sup instability (see, for instance, Hidano et al. [26]).

The source of the inf-sup instability is the selected combination of spaces for the displacement and the pressure fields (i.e., the violation of the Ladyzhenskaya-Babuška-Brezzi (LBB) condition). There are a number of solutions to this issue in the literature. Taylor-Hood elements [27] employ higher-order interpolant functions for the displacement field while using lower ones for the pressure field. While attractive when using high-order interpolant functions, Taylor-Hood elements do not represent the best options when lower-order functions are desired. Formulations using reduced integration schemes (see e.g., [28]) are particularly attractive for ease of implementation. However, these solutions cannot fully solve the pressure oscillation in proximity to nearly undrained conditions (see [24]). Stabilised formulations (see, for instance, [22, 29]) represent an alternative way to comply with the LBB condition, which is achieved by adding a stabilising term to the set of primary equations. Since these terms often are pre-multiplied by a constant quantity (which guarantees the compliance of the physical units with the other terms in the equations), it can be difficult to select these values, especially in correspondence with non-linear behaviour. Moreover, these stabilising terms represent an additional computational cost not required by the physical laws governing the problem. Another option is to adopt stable-by-design elements, such as Qk$_{SD}$-Qk elements (where the subscript SD stands for Sub-$Divided$, while k is the degree of the shape functions polynomials). These employ the same order of interpolant function for the displacement and the pressure field on meshes of different sizes. In particular, the mesh used for the displacement field has a characteristic length of half that of the mesh employed for the pressure. This solution is particularly attractive when low-order shape functions are desired, which motivates their use for an implicit formulation in this manuscript.

Another important consideration is that an MP-based discretisation inevitably leads to small overlaps between the stencils of the shape functions and the physical domain of the MPs (and their role as quadrature points; see [30]). In the literature, this problem often goes under the name of the *small-cut* problem, which represents a second source of instability for the MPM tackled in this paper. If the overlap between the shape function's stencil and the physical MP-based domain is practically infinitesimal, the system matrix can become ill-conditioned. A possible remedy coming from the unfitted FEM literature, that is, the *ghost penalty method*, is therefore introduced and adapted to the Qk$_{SD}$-Qk formulations under consideration. It must be noted that these two sources of instabilities (i.e., the inf-sup condition and the small cut issue) are not restricted to the MPM and to a $u - p^{(f)}$ formulation for poromechanics: similar findings have been pointed out, for instance, by Burman and Hansbo [31] in the context of unfitted FEM for Stokes problems and the applicability of the methodologies discussed in this manuscript go well beyond the MPM.

After briefly introducing mixture theory in Section 2, Section 3 of this manuscript is devoted to illustrating the necessary requirements for solvability in the continuum context. These include compliance with the inf-sup condition and the effects that the small-cut issue causes in regard to these requirements. Section 4 introduces the MPM algorithm. Following this, a description of the small-cut issue in the MPM context follows in Section 4.2 and a remedy proposed in Section 4.3. Section 4.4 is devoted to the design of a stable MPM Qk$_{SD}$-Qk formulation, which includes linear Lagrange polynomial functions and GIMPM (Generalised Interpolation MPM, see, for instance, [32, 33]) interpolant functions. Two- and three-dimensional examples are given in Section 5.

It must be noted that the lack of a formal analysis (see, for instance, Nguyen et al. [34]) of the MPM inhibits some results, which are pivotal and well-acknowledged in the FEM theory. However, the similarities between the two methods can be quite substantial in some aspects. This point has been raised by different authors (see, for instance, [35, 36]), especially in light of seeing the MPM as a FEM where quadrature points are allowed to move independently from the mesh across different time steps. Exploiting these similarities in some circumstances permits us to refer to functional analysis and the (unfitted) FEM theory and inherit results that, even if not formally applicable, are practically helpful in the MPM context. This idea of falling back to the FEM theory for MPM analyses, even if not rigorous, is motivated by rationales provided throughout the paper and supported by numerical examples in Section 5.

2 | Fundamentals of Mixture Theory

To formalise the mechanics of a two-phase (solid/fluid) material modelled with one set of MPs, this section briefly details the underlying continuum formulation for mixture theory.

2.1 | Kinematics of the Phases

The kinematics assumptions considered in this work are as follows:

1. the fully saturated porous material is treated as two (solid and fluid) juxtaposed continua;

2. for simplicity, only one fluid material constitutes this phase;

3. thermal effects and viscosity are neglected; and

4. the porous material undergoes finite strains and rotations in the elasto-plastic regime.

Having introduced the founding assumptions, let the mixed body $\mathcal{B}$ occupy a volume Ω in the original configuration (at time $t = 0$) and a volume ω in the current configuration (at the generic time t). Owing to Assumption 1, each infinitesimal volume belonging to a mixed body contains a solid and a unique (as implied by Assumption 2) fluid phase. These phases are mapped through the different configurations via the invertible mappings $\varphi^{(ph)}\big(X^{(ph)}, t\big)$, with $ph = s, f$ (standing for solid and fluid), and $X^{(ph)}$ indicating the initial position of each phase. These continua can evolve differently in different configurations over time, which raises the question of which phase to trace. In this sense, the mapping of the solid configuration is *de facto* privileged over the mapping of the fluid phase, which is mostly indirectly traced by considering the relative velocity between the phases. Given this consideration, the solid material particle of initial mixed volume $d\Omega$ occupies a volume $d\omega = J \, d\Omega$ in the current configuration, where the Jacobian J is given by the determinant of the solid phase deformation gradient[1], this being

$$F \cdot dX^{(s)} = dx, \quad \text{with } F_{iI} = \frac{\partial \varphi_i^{(s)}}{\partial X_I^{(s)}}. \tag{1}$$

In the above equation, x denotes the material particle position in the current configuration obtained using the solid mapping

(i.e., $x = \varphi^{(s)}(X^{(s)}, t)$). The indices $i = 1, \ldots, 3$ and $I = 1, \ldots, 3$ indicate the components of the matching Cartesian basis vectors $e_i = E_I$ in the current (e_i) and reference (E_I) configurations.

As proposed by Kröner [37], Lee [38] and Mandel [39] and considered in Assumption 4, the deformation gradient is multiplicatively decoupled into an elastic and plastic part as follows

$$F = F^e \cdot F^p \tag{2}$$

where, due to Assumption 3, no other effects contribute to the deformation gradient. Other measures of strain used in this work are based on the deformation gradient (or its elastic/plastic part), such as the *left Cauchy-Green strain* $b := F \cdot F^T$ and the logarithmic strain $\epsilon := \frac{1}{2} \ln b$.

To describe the volume fractions of each phase, the Eulerian porosity n is defined as the ratio between the current fluid volume of the material particle $d\omega^{(f)}$ and its current mixed volume $d\omega$, that is, $n := \frac{d\omega^{(f)}}{d\omega}$. E contrario, $(1 - n)$ gives the volume fraction of the material particle occupied by the solid phase, that is, $(1 - n) = \frac{d\omega^{(s)}}{d\omega}$. The initial value of the Eulerian porosity is denoted by n_0. As can be seen, the Eulerian porosity satisfies the property

$$0 < n < 1 \tag{3}$$

where the extremes are excluded to always consider coexisting phases in the material.

The *displacements* are defined as the difference between the current and the original positions. Given the choice of matching Cartesian basis vectors, displacements can be defined as

$$u^{(ph)} := \varphi^{(ph)}\big(X^{(ph)}, t\big) - X^{(ph)}. \tag{4}$$

The total time derivative of the current position gives the *material velocities*

$$v^{(ph)} := \frac{d}{dt}\bigg|_{(ph)} \varphi\big(X^{(ph)}, t\big) \tag{5}$$

where $\frac{d}{dt}\big|_{(ph)} (\bullet)$ indicates the time derivative of $(\bullet)$ following the $ph -$ phase.

2.2 | Mass Conservation

On top of the principle of mass conservation, these further assumptions are introduced:

5. the constituents do not exchange mass;

6. both constituents are incompressible; and

7. the porosity network is homogeneous and connected across the material.

Assumption 5 permits writing the conservation of the mixture separately for each phase, that is,

$$\frac{d}{dt}\bigg|_{(s)} \int_{\omega^{(s)}} \rho^{(s)}(1 - n) dv = 0 \tag{6}$$

$$\frac{d}{dt}\bigg|_{(f)} \int_{\omega^{(f)}} \rho^{(f)} n \, dv = 0 \tag{7}$$

where $\rho^{(ph)}$ indicates the *mesoscopic density* of the $ph-$ phase, which, according to Assumption 6, is constant, that is, $\rho^{(ph)} = \rho_0^{(ph)}$. The exclusion of a double porosity network by Assumption 7 allows the fluid mass balance to be written as in Equation (7), that is, considering only one type of porosity, approximately homogeneous in size and shape in the medium under investigation. Owing to the arbitrary nature of the integration volume and the incompressibility of the solid phase (part of Assumption 6), Equation (6) can also be expressed as follows

$$n = 1 - \frac{1}{J}\left(1 - n_0\right). \tag{8}$$

Two other equations are employed to express Equation (7) in a convenient way. The former is given by the relationship between material time derivatives relative to the two different phases (see Thorpe [40]), that is,

$$\left.\frac{d}{dt}\right|_{(f)}(\bullet) = \left.\frac{d}{dt}\right|_{(s)}(\bullet) + \mathbf{grad}(\bullet) \cdot \left(\mathbf{v}^{(f)} - \mathbf{v}^{(s)}\right) \tag{9}$$

where **grad** indicates the gradient with respect to the current position $\mathbf{x}$. The second equation stems from the property relative to the derivation of determinants of second-order tensors, and it is given by

$$\left.\frac{d}{dt}\right|_{(ph)} J = J \ \mathbf{div} \cdot \mathbf{v}^{(ph)} \tag{10}$$

where **div** is the divergence with respect to the current position $\mathbf{x}$. Invoking the arbitrary nature of the integration domain again, and using Equations (8) to (10), the fluid mass conservation given by Equation (7) can be re-written as

$$\rho_0^{(f)} \left.\frac{dJ}{dt}\right|_{(s)} + J \ \mathbf{div} \cdot \mathbf{q}^{(f)} = \rho_0^{(f)} \dot{J} + J \ \mathbf{div} \cdot \mathbf{q}^{(f)} = 0 \tag{11}$$

where the shorthand notation $(\dot{\bullet}) = \left.\frac{d}{dt}\right|_{(s)}(\bullet)$ and $\mathbf{q}^{(f)}$ is the relative flux defined as

$$\mathbf{q}^{(f)} := \rho_0^{(f)} \ n\left(\mathbf{v}^{(f)} - \mathbf{v}^{(s)}\right). \tag{12}$$

2.3 | Balance of Rate of Linear Momentum

Let us further assume that

8. inertia effects are negligible.

Under this Assumption 8, the balance of the rate of the linear momentum for the mixed body can be expressed as follows

$$\mathbf{div} \cdot \boldsymbol{\sigma} + \rho \ \mathbf{b} = \mathbf{0} \tag{13}$$

where $\boldsymbol{\sigma}$ is the *total Cauchy stress*, $\rho := \rho_0^{(s)}(1 - n) + \rho_0^{(f)} \ n$ is the *current density of the porous material*, and $\mathbf{b}$ are the body forces per unit mixed weight. The stress introduced in the above equation can be further characterised. As demonstrated by Borja and Alarcón [41], considering a perfect fluid (included in Assumption 3) and an incompressible solid phase (Assumption 6) allows the *Terzaghi effective stress decomposition*[2] to hold even in the finite strain context, this being

$$\boldsymbol{\sigma} = \boldsymbol{\sigma}' - p^{(f)}\mathbf{1} \tag{14}$$

where **1** is the second-order identity tensor. In the above equation and throughout this manuscript, the dash $(\bullet)'$ denotes the *effective* quantities of stress, that is, those obeying a constitutive relationship with the solid strains $\boldsymbol{\sigma}'(\mathbf{u}^{(s)})$, while $p^{(f)}$ is the *Cauchy fluid pressure*.

2.4 | Constitutive Relationships

To introduce the necessary constitutive relationships, it is assumed that

9. the material is isotropic; and

10. the fluid flow exhibits Low Reynolds number.

Assumption 9 has two consequences. On the one hand, it results in *isotropic* elasto-plastic behaviour relating the effective stress and the solid strains. In particular, this work adopts the *improved Hencky material* suggested in Pretti et al. [42] to avoid negative values of the Eulerian porosity and to conserve solid mass. The effective free energy function Ψ' per unit initial volume of this material is given by

$$\Psi'(\boldsymbol{\epsilon}, \boldsymbol{\alpha}) = \frac{K}{2 \ n}\left(\epsilon_v^e\right)^2 + \frac{3}{2}G\left(\epsilon_q^e\right)^2 + \tilde{\Psi}'(\boldsymbol{\alpha}) \tag{15}$$

where $K > 0$ and $G > 0$ are the bulk parameter and the shear modulus, while $\tilde{\Psi}'$ defines a part of the free energy function responsible for the kinematic hardening, based on a set of internal variables $\boldsymbol{\alpha}$. A few invariants of the logarithmic strains have also been employed in the above equation, which are defined as

$$\epsilon_v := \boldsymbol{\epsilon} : \mathbf{1}; \qquad \mathbf{e} := \boldsymbol{\epsilon} - \frac{\epsilon_v}{3}\mathbf{1}; \qquad \epsilon_q := \sqrt{\frac{2}{3} \ \mathbf{e} : \mathbf{e}} \tag{16}$$

with : being the double contraction operator between tensors. If isotropic permeability is assumed (consequence of Assumptions 7 and 9) together with Assumption 10, the *Darcy-Weisbach* law relates the relative flux to the fluid pressure gradient and body forces as follows

$$\mathbf{q}^{(f)} = -\frac{\kappa}{g}\left(\mathbf{grad} \ p^{(f)} - \rho_0^{(f)}\mathbf{b}\right) \tag{17}$$

with κ being the *hydraulic conductivity* and g the magnitude of the gravitational force. The *Kozeny-Carman* formula is assumed to account for the dependency of the hydraulic conductivity on the porosity, that is,

$$\kappa = c_1 \frac{n^3}{(1 - n)^2} \tag{18}$$

with c_1 being a constant parameter. As for the fluid constitutive behaviour, Assumption 3 excludes the dependence of the fluid part on the viscosity, indicating that the fluid cannot bear any deviatoric stress. However, as embedded in Assumption 6, the fluid pressure is also unrelated to any constitutive relationship, thus entirely ruling out a constitutive behaviour for the fluid phase. This circumstance was discussed by Miehe et al. [43], who recognised the role played by the fluid pressure as a Lagrange multiplier that shifts the dependency of stresses on strain (i.e., the idea of effective stress) depending on the water mass conservation constraint (i.e., drained/undrained conditions). This observation

has direct consequences on the mapping processes detailed in Section 4.6, since the fluid pressure does not relate to any form of energy.

3 | Continuum Weak Form and Arising Requirements

This section introduces a weak statement of the equations for a $\boldsymbol{u} - p^{(f)}$ formulation, which results in a saddle point formulation (Section 3.1). As is well-acknowledged, this kind of problem can be solved only under specific conditions.

3.1 | From Strong to Weak Form of Equations

The primary equations employed in an updated Lagrangian $\boldsymbol{u} - p^{(f)}$ formulation are given by the mixture equilibrium Equation (13) and the fluid mass conservation Equation (11), these being

$$\mathbf{div} \cdot \left(\boldsymbol{\sigma}' - p^{(f)} \, \mathbf{1} \right) + \rho \, \boldsymbol{b} = \mathbf{0} \quad \text{in} \ \ \omega \tag{19}$$

$$\rho_0^{(f)} \boldsymbol{j} - J \, \mathbf{div} \cdot \left(\frac{\kappa}{g} \left(\mathbf{grad} \, p^{(f)} - \rho_0^{(f)} \boldsymbol{b} \right) \right) = 0 \quad \text{in} \ \ \omega^{(f)} \tag{20}$$

where the Terzaghi effective stress decomposition Equation (14) and the Darcy-Weisbach law Equation (17) have been substituted. The current boundary $\gamma = \partial\omega$ of the considered mixed body is partitioned as follows

$$\gamma = \gamma^{\bar{u}} \cup \gamma^{\bar{t}} = \gamma^{\bar{p}} \cup \gamma^{\bar{q}} \tag{21}$$

$$\gamma^{\bar{u}} \cap \gamma^{\bar{t}} = \emptyset = \gamma^{\bar{p}} \cap \gamma^{\bar{q}} \tag{22}$$

where $\gamma^{(\bullet)}$ is a particular portion of the boundary. Prescribed boundary conditions (BCs) are given on these parts and are as follows

$$\boldsymbol{u} = \bar{\boldsymbol{u}} \qquad \text{on} \ \gamma^{\bar{u}} \tag{23}$$

$$\boldsymbol{\sigma} \cdot \boldsymbol{n} = \bar{\boldsymbol{t}} \qquad \text{on} \ \gamma^{\bar{t}} \tag{24}$$

$$p^{(f)} = \bar{p} \qquad \text{on} \ \gamma^{\bar{p}} \tag{25}$$

$$\boldsymbol{q}^{(f)} \cdot \boldsymbol{n} = \bar{q} \qquad \text{on} \ \gamma^{\bar{q}}. \tag{26}$$

The above equations constitute the Dirichlet, Equations (23) and (25), and the Neumann, Equations (24) and (26), BCs for the mixture equilibrium (19) and fluid mass conservation (20), respectively.

The weak form of the above problem is obtained by introducing test functions belonging to the required function spaces and integrating over the relative domains[3]. By applying the divergence theorem and using Neumann BCs (24) and (26), the weak form can be stated as follows: find $\boldsymbol{u} \in \mathcal{V}_{\bar{u}}$ and $p^{(f)} \in \mathcal{W}_{\bar{p}}$ such that, for $t \in [0, \tilde{t}]$,

$$\delta\Pi^{eq}\left((\boldsymbol{u}; p^{(f)}); \delta\boldsymbol{w}\right) := \int_{\omega} \mathbf{grad}(\delta\boldsymbol{w}) : (\boldsymbol{\sigma}' - p^{(f)}\mathbf{1}) dv$$
$$- \int_{\omega} \rho\delta\boldsymbol{w} \cdot \boldsymbol{b} dv - \int_{\gamma^{\bar{t}}} \delta\boldsymbol{w} \cdot \bar{\boldsymbol{t}} da = 0, \qquad \forall \delta\boldsymbol{w} \in \mathcal{V}_{\mathbf{0}} \tag{27}$$

$$\delta\Pi^{cons}\left((\boldsymbol{u}; p^{(f)}); \delta\eta\right) := \int_{\omega} \rho_0^{(f)} \delta\eta \frac{\boldsymbol{j}}{J} dv$$
$$+ \int_{\omega} \frac{\kappa}{g} \mathbf{grad}(\delta\eta) \cdot \left(\mathbf{grad} p^{(f)} - \rho_0^{(f)} \boldsymbol{b} \right) dv - \int_{\gamma^{\bar{q}}} \delta\eta \bar{q} da = 0, \qquad \forall \delta\eta \in \mathcal{W}_{\mathbf{0}} \tag{28}$$

giving the initial condition $\boldsymbol{u}(t = 0) = \boldsymbol{u}_0$. The potentials Π^{eq} and Π^{cons} and their first variation $\delta(\bullet)((\dots); \delta(\tilde{\bullet}))$ with respect to their argument $(\tilde{\bullet})$ have been above employed, while the spaces of trial functions are defined as follows

$$\mathcal{V}_{\bar{u}} = \left\{ \boldsymbol{u} \in \left[H^1(\omega) \right]^{n^{\dim}} \middle| \boldsymbol{u} = \bar{\boldsymbol{u}} \ \text{on} \ \gamma^{\bar{u}} \right\} \tag{29}$$

$$\mathcal{W}_{\bar{p}} = \left\{ p^{(f)} \in \left[H^1(\omega) \right] \middle| p^{(f)} = \bar{p} \ \text{on} \ \gamma^{\bar{p}} \right\} \tag{30}$$

where $H^1(\omega)$ denotes the Sobolev space of degree one on ω. The spaces of the test functions $\delta\boldsymbol{w}$ and $\delta\eta$ are denoted by $\mathcal{V}_{\mathbf{0}}$ and $\mathcal{W}_{\mathbf{0}}$ and follow similar definitions as the above, with the exception of being zero on the Dirichlet boundary. It is well-known (see, for instance, Dortdivanlioglu et al. [44]) that the above weak problem Equations (27) and (28) can be given by the stationarity of the following saddle point problem

$$\inf_{\boldsymbol{w} \in \mathcal{V}_{\mathbf{0}}} \sup_{q \in \mathcal{W}_{\mathbf{0}}} \Pi(\boldsymbol{w}; \eta) \tag{31}$$

with $\Pi(\boldsymbol{w}; \eta) = \Pi^{eq}(\boldsymbol{w}; \eta) - \Pi^{cons}(\boldsymbol{w}; \eta)$.

3.2 | Linearisation

Equations (27) and (28) represent a non-linear system of equations in $\boldsymbol{u}$. This is primarily due to having set the problem in the context of finite strain mechanics. On top of this, other non-linearities, such as elasto-plastic behaviour or constitutive equation (15), can be included too. To solve these equations, the Newton-Raphson (NR) method stipulates that linearisation of Equations (27) and (28) at a solution $(\breve{\boldsymbol{u}}; \breve{p}^{(f)})$ is required, this being

$$0 = \delta\Pi((\breve{\boldsymbol{u}}; \breve{p}^{(f)}); (\delta\boldsymbol{w}, \delta\eta))$$
$$\approx \delta\Pi\left((\boldsymbol{u}; p^{(f)}); (\delta\boldsymbol{w}, \delta\eta)\right) + \delta((\delta\Pi((\boldsymbol{u}; p^{(f)}); (\delta\boldsymbol{w}, \delta\eta))); (\delta\boldsymbol{u}, \delta p^{(f)}))$$
$$= \delta\Pi^{eq}((\boldsymbol{u}; p^{(f)}); (\delta\boldsymbol{w})) - \delta\Pi^{cons}((\boldsymbol{u}; p^{(f)}); (\delta\eta))$$
$$+ \delta((\delta\Pi^{eq}((\boldsymbol{u}; p^{(f)}); \delta\boldsymbol{w})); (\delta\boldsymbol{u}, \delta p^{(f)})) - \delta((\delta\Pi^{cons}((\boldsymbol{u}; p^{(f)}); \delta\eta)); (\delta\boldsymbol{u}, \delta p^{(f)})). \tag{32}$$

The second variations appearing in the above equations can be expressed as follows

$$\delta((\delta\Pi^{eq}((\boldsymbol{u}; p^{(f)}); \delta\boldsymbol{w})); (\delta\boldsymbol{u}, \delta p^{(f)})) - \delta((\delta\Pi^{cons}((\boldsymbol{u}; p^{(f)}); \delta\eta)); (\delta\boldsymbol{u}, \delta p^{(f)}))$$
$$= \begin{bmatrix} \delta\boldsymbol{w}, \delta\eta \end{bmatrix} \underbrace{\begin{bmatrix} \mathbf{A} & \mathbf{B}^{(1)} \\ \mathbf{B}^{(2)} & \mathbf{C} \end{bmatrix}}_{:= \mathbf{J}} \begin{bmatrix} \delta\boldsymbol{u} \\ \delta p^{(f)} \end{bmatrix} \tag{33}$$

where $\mathbf{J}$ indicates the Jacobian matrix. Under the assumptions made so far, the submatrix $\mathbf{C}$[4] is symmetric, that is, $\mathbf{C} = \mathbf{C}^T$.

In the small strain regime, the above linear system also satisfies the useful properties $\mathbf{A} = \mathbf{A}^T$ and $\left(\mathbf{B}^{(1)}\right)^T = \mathbf{B}^{(2)}$. In this context, the Jacobian matrix can exhibit two situations that are well-acknowledged for saddle-point problems. On the one hand,

in the case of drained or partially drained processes, the above Jacobian is as follows

$$\mathbf{J} = \begin{bmatrix} \mathbf{A} & \mathbf{B}^T \\ \mathbf{B} & \mathbf{C} \end{bmatrix}. \tag{34}$$

The solvability (uniqueness of solution) of the above linear system is guaranteed if the bilinear forms associated with the submatrices $\mathbf{A}$ and $\mathbf{B}$ are continuous, and $\mathbf{A}$ and $\mathbf{C}$ are coercive (see, for instance, Boffi et al. [45], Proposition 4.3.1). On the other hand, the process can take place in nearly undrained conditions. Physically speaking, these circumstances can occur when load rates are rapidly applied with low values of hydraulic conductivity or when BCs do not allow for drainage. These cases result in the following Jacobian

$$\mathbf{J} = \begin{bmatrix} \mathbf{A} & \mathbf{B}^T \\ \mathbf{B} & \epsilon\,\tilde{\mathbf{C}} \end{bmatrix} \tag{35}$$

where $\mathbf{C} = \epsilon\,\tilde{\mathbf{C}}$ with $0 < \epsilon \ll 1$ indicates that the submatrix $\mathbf{C}$ contains small entries compared to the other submatrices. In the above condition, solvability is guaranteed (see, e.g., Boffi et al. [45], Theorem 4.3.4) if the bilinear form associated with $\mathbf{A}$ and $\mathbf{C}$ is continuous and $\mathbf{A}$ is coercive. Furthermore, the solution to Equation (35) is stable if $\mathbf{B}^T$ is such that its bilinear form satisfies the *inf-sup* condition, that is,

$$\inf_{(\delta\eta\in\mathscr{W}_0)} \sup_{(\delta\boldsymbol{w}\in\mathscr{V}_0)} \frac{\int_\omega \delta\eta\,\mathbf{div}\cdot\delta\boldsymbol{w}\,dv}{\|\delta\eta\|_{H^0}\,\|\delta\boldsymbol{w}\|_{\mathscr{V}_0}} \geq \alpha > 0 \tag{36}$$

where the L-2 norm $\|(\bullet)\|_{H^0}$ must be considered even for poro-mechanical problems (see the discussions in Mira et al. [46] and Dortdivanlioglu et al. [44]). Furthermore, the use of this norm in Equation (36) allows use of the numerical test proposed by Chapelle and Bathe [47] for incompressible elasticity or Stokes problems.

From the above discussions on drained and undrained cases, it emerges that three requirements are necessary for inverting the Jacobian matrix without incurring unstable solutions (neglecting for the moment the continuity of bilinear forms of submatrices $\mathbf{A}$ and $\mathbf{C}$). These conditions are the coercivity of the bilinear forms associated with $\mathbf{A}$ and $\mathbf{C}$, and the satisfaction of the inf-sup condition for the bilinear form associated with $\mathbf{B}$.

It must also be stressed that adopting the improved Hencky material defined by Equation (15) has important consequences for the coercivity of $\mathbf{C}$, since it avoids negative values of the Eulerian porosity, as detailed in Pretti et al. [42]. While this criterion does not come from the numerical requirements of the problem under investigation, its physically based nature substantially affects numerical outcomes. This constraint and its relative consequences hold even in the case of compressible material. In this case, the reader is invited to refer to the work of Nedjar [48, 49] on circumventing negative values in Eulerian porosity. Owing to the adoption of the improved Hencky material in this work, this physical constraint will not be discussed further.

4 | Stable MPM Discretisation

This section introduces an MPM $\boldsymbol{u} - p^{(f)}$ formulation and discusses when the conditions for solvability introduced in the previous section are not fulfilled. Remedies to mitigate the effects of these losses are also proposed.

4.1 | MPM Algorithm

Figure 1 shows the phases in the overall MPM algorithm. The MPM-based discretisation stipulates that the considered body of global volume ω is discretised by a cloud of Material Points (MPs), that is, $\omega \approx \cup_{mp=1}^{N^{mp}} {}^{mp}\omega := {}^{MP}\omega$; the MPs carry all the information necessary to run the analysis. These points are immersed into a (usually Cartesian) grid/mesh $\mathcal{T}$ discretising a portion of the Euclidean space $\mathcal{E}$ of $n^{\dim}$ dimensions, which fully contains the considered body ω (Phase (i) in Figure 1).

Finite-dimensional test and trial functions are defined on a mesh of generic length $\check{h}$. $\check{h}$, when employed as a superscript, denotes finite-dimensional quantities. The trial and test functions are interpolated with the help of nodal shape functions, similar to the FEM. The finite-dimensional spaces of the trial functions are given by

$$^{\check{h}}\mathscr{V}_{\bar{\boldsymbol{u}}} = \left\{ {}^{\check{h}}\boldsymbol{u} \in \left[C^m\left({}^{\check{h}}\overline{\omega}\right) \right]^{n^{\dim}} \middle| {}^{\check{h}}\boldsymbol{u}(\boldsymbol{x}) = \mathrm{N}_a^{\check{h},u}(\boldsymbol{x})\mathbf{u}_a \right.$$
$$\left. \text{with } a \in \mathrm{clos}\left({}^{\check{h}}\mathcal{T}^{\mathrm{act}}\right),\ {}^{\check{h}}\boldsymbol{u} = \overline{\boldsymbol{u}} \text{ on } {}^{\check{h}}\overline{\gamma}^{\bar{u}} \right\} \tag{37}$$

$$^{\check{h}}\mathscr{W}_{\bar{p}} = \left\{ {}^{\check{h}}p^{(f)} \in C^m\left({}^{\check{h}}\overline{\omega}\right) \middle| {}^{\check{h}}p^{(f)}(\boldsymbol{x}) = \mathrm{N}_a^{\check{h},p}(\boldsymbol{x})\,\mathrm{p}_a \text{ with } a \in \mathrm{clos}\left({}^{\check{h}}\mathcal{T}^{\mathrm{act}}\right) \right\} \tag{38}$$

where $^{\check{h}}\overline{\omega} = \left(\bigcup_{T\in {}^{\check{h}}\mathcal{T}^{\mathrm{act}}} T\right)$ denotes the volume defined by the set of active grid elements $^{\check{h}}\mathcal{T}^{\mathrm{act}}$, that is,

$$^{\check{h}}\mathcal{T}^{\mathrm{act}} = \{T\in {}^{\check{h}}\mathcal{T} \mid \exists\ mp\ :\ \mathrm{N}_a^{\check{h}}({}^{mp}\boldsymbol{x}) > 0\ \forall a \in \mathrm{clos}(T)\} \tag{39}$$

with $\mathrm{N}_a^{\check{h}}$ being the generic low-order shape functions at the a-th node belonging to the element T and $\mathrm{clos}(\bullet)$ denotes the closure of the entity $(\bullet)$[5]. As detailed below in Section 4.4, this work assumes two kinds of shape functions. The first choice is given by first-order Lagrange polynomials, and results in $C^0({}^{\check{h}}\overline{\omega})$ functions (i.e., $m = 0$). Since they were first adopted in the original MPM formulation (see Sulsky et al. [1, 2]), these shape functions are labelled sMPM (standard MPM). On the other hand, GIMPM shape functions, resulting in piecewise first-order and second-order polynomials, are also considered, giving $C^1({}^{\check{h}}\overline{\omega})$ functions (i.e., $m = 1$).

To initialise the grid with the required information, a mapping from the MPs to the grid nodes is usually required (Phase (ii) in Figure 1). This procedure is named Point-2-Grid (P2G) mapping and, for the current formulation, is addressed in Section 4.6.

The (standard) assembly process of the Lagrangian equations (Phase (iii) in Figure 1) takes place at the grid nodes and employs the MPs as quadrature points. In the case of the considered $\boldsymbol{u} - p^{(f)}$ formulation, the equations become (dropping the dependencies from the position)

$$\int_{MP_\omega} \delta\mathbf{w}_a\,\mathbf{grad}\left(\mathrm{N}_a^{\check{h},u}\right) : \left(\boldsymbol{\sigma}' - \mathrm{N}_b^{\check{h},p}\,\mathrm{p}_b\,\mathbf{1}\right) dv$$
$$- \int_{MP_\omega} \left(\delta\mathbf{w}_a\,\mathrm{N}_a^{\check{h},u}\right)\cdot\rho\boldsymbol{b}\,dv - \int_{\gamma^{\bar{t}}} \left(\delta\mathbf{w}_a\,\mathrm{N}_a^{\check{h},u}\right)\cdot\bar{\boldsymbol{t}}\,da = 0, \quad \forall\delta\mathbf{w}_a \in {}^{\check{h}}\mathscr{V}_{\mathbf{0}} \tag{40}$$

$$\int_{MP_\omega} \left(\delta\eta_a\,\mathrm{N}_a^{\check{h},p}\right)\rho_0^{(f)}\frac{\dot{J}}{J}\,dv$$
$$+ \int_{MP_\omega} \frac{\kappa}{g}\,\delta\eta_a\,\mathbf{grad}\left(\mathrm{N}_a^{\check{h},p}\right)\cdot\left(\mathbf{grad}\left(\mathrm{N}_b^{\check{h},p}\right)\mathrm{p}_b - \rho_0^{(f)}\boldsymbol{b}\right)dv - \int_{\gamma^{\bar{q}}} \left(\delta\eta_a\,\mathrm{N}_a^{\check{h},p}\right)\overline{q}\,da$$
$$+ \gamma^{\mathrm{pen}}\int_{\gamma^{\bar{p}}} \left(\delta\eta_a\,\mathrm{N}_a^{\check{h},p}\right)\left(\mathrm{N}_b^{\check{h},p}\,\mathrm{p}_b - \overline{p}\right)da = 0, \quad \forall\delta\eta_a \in {}^{\check{h}}\mathscr{W}_0 \tag{41}$$
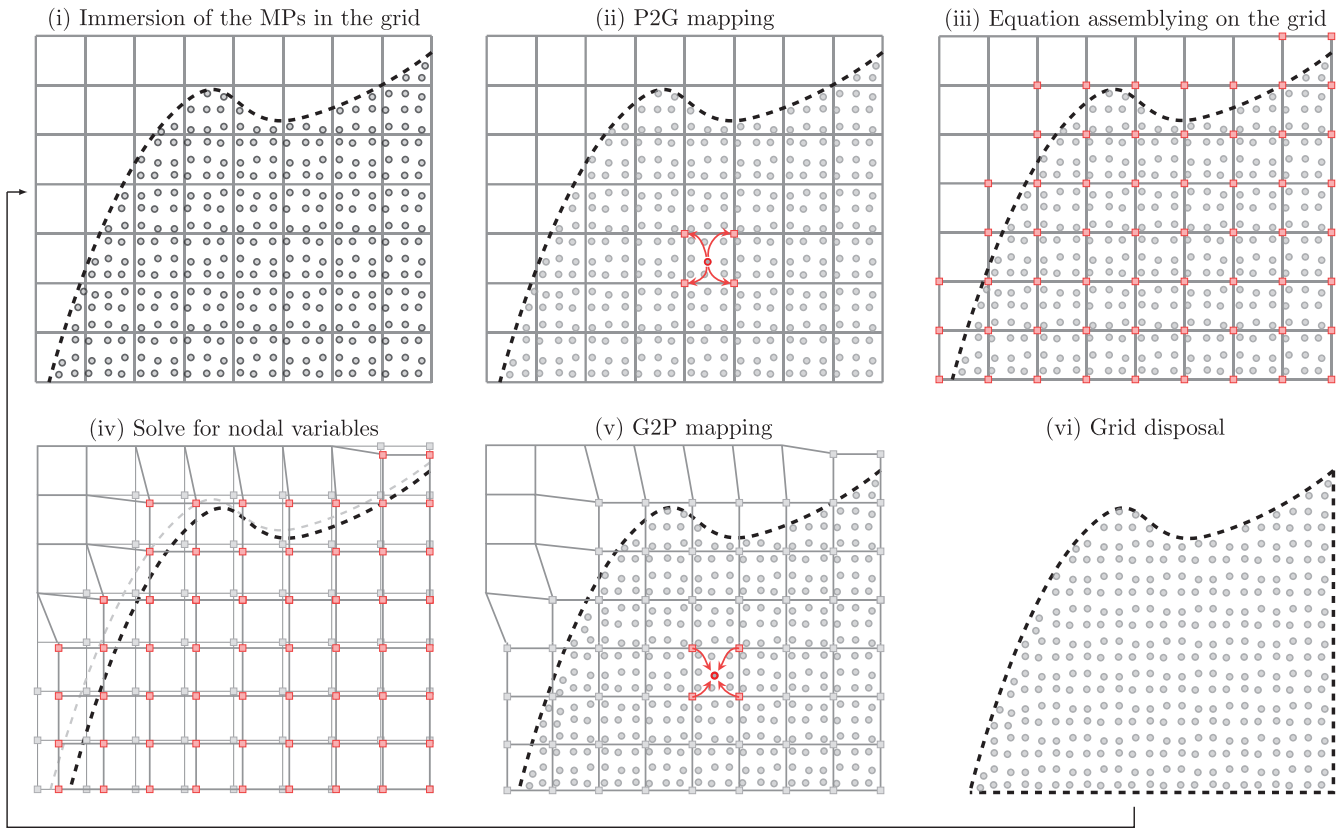
FIGURE 1 | MPM step phases. (i) Immersion of the MPs in the grid. (ii) P2G mapping. (iii) Equation assemblying on the grid. (iv) Solve for nodal variables. (v) G2P mapping. (vi) Grid disposal.

where the volume integrals are approximated as follows

$$\int_{MP_\omega} (\bullet) dv \approx \sum_{mp=1}^{N^{mp}} {}^{mp}\omega(\bullet(^{mp}x)). \qquad (42)$$

As for the boundary integrals, this work follows the procedure explained by Bird et al. [50], leveraging the MPs' corners (see Bird et al. [50] for more details). This method is also exploited for non-conforming pressure Dirichlet BCs, represented by the penalty term in Equation (41), with γ^{pen} being a penalty parameter. Conversely, this work always considers mesh-conforming displacement BCs, as assumed in Equation (37). Equations (40) and (41) are solved for the nodal unknowns (Phase (iv) in Figure 1), and this work considers an iterative Newton-Raphson (NR) scheme based on the discrete counterpart of Equation (32) (see Appendix A). Since the updated solution lies on the grid, a subsequent mapping from this to the MPs is required to update the solution at the MPs level (Phase (v) in Figure 1). This is called the Grid-2-Point (G2P) mapping and is discussed in Section 4.6. The grid is discarded at the end of the step (Phase (vi) in Figure 1), and a further step can start with an undistorted grid.

4.2 | The Small-Cut Issue in the MPM

As clear from the description of the phases of the MPM, the immersion of the clouds of MPs into a mesh and their use

as quadrature points generates an intrinsically unfitted method since $^{MP}\omega \subseteq \,^{\tilde{h}}\overline{\omega}$. Moreover, an extremely small overlap between the shape function's stencil and the MP's domains can lead to ill-conditioned systems. This problem, named the small-cut issue is exacerbated especially for those elements on the domain's boundaries. As demonstrated by Burman [51] in the context of unfitted FEM, this issue provokes the loss of the coercivity for the bilinear forms computed on these elements and the consequent impossibility of solving the relative linear (or linearised) system of equations.

To manage this issue, Burman [51] has proposed adding a penalty term, named the ghost penalty stabilisation, which extends the coercivity of the bilinear forms to the partially filled boundary elements. While strictly enforcing coercivity in an MPM formulation is difficult to prove (properties such as continuity or coercivity rely on norms that, in turn, are based on quadrature rules more precise than Equation (42)), it is nonetheless possible to limit the condition number of the matrices by the use of the ghost penalty method (see Coombs [30]). The addition of the ghost penalty restores to some degree coercivity on those elements suffering from the small-cut issue. Hence, while formalisms must be dropped for the above-mentioned causes, MPM-based discrete linear systems can be inverted independently from the small-cut issue, as long as the ghost penalty (or a similar technique, see the discussion in Section 4.3) is introduced.

Among the ghost penalties introduced in the literature for the unfitted FEM (see Burman et al. [52]), the *face* ghost penalty[6] has been introduced to the MPM by Coombs [30], and an extension to a $\boldsymbol{u} - p^{(f)}$ formulation for the unfitted FEM has been proposed by Liu et al. [53]. The following section extends the face ghost stabilisation for the $\boldsymbol{u} - p^{(f)}$ MPM formulations introduced above.

4.3 | Face Ghost Stabilisation

In the case of low-order shape functions, the face ghost stabilisation states that the following bilinear form must be added to the considered primary equations, that is,

$$j^F \left({}^{\bar{h}}\delta\boldsymbol{v}, {}^{\bar{h}}\boldsymbol{v} \right) := \tilde{h} \int_{{}^{\bar{h}}\gamma^F} \left[\left[\left(\mathbf{grad}\left({}^{\bar{h}}\delta\boldsymbol{v} \right) \cdot \mathbf{n} \right) \right] \right] \cdot \left[\left[\left(\mathbf{grad}\left({}^{\bar{h}}\boldsymbol{v} \right) \cdot \mathbf{n} \right) \right] \right] da \quad (43)$$

where ${}^{\bar{h}}\boldsymbol{v}$ and ${}^{\bar{h}}\delta\boldsymbol{v}$ are the generic trial and test functions and $[[\mathbf{grad}(\bullet) \cdot \mathbf{n}]]$ is the jump in the normal gradient across a shared facet F. The procedure to select these facets (listed in $\mathscr{F}$) describing the surface ${}^{\bar{h}}\gamma^F$ is outlined in Algorithms 1 and 2. In particular, since the MPM retains no explicit representation of the boundary, Algorithm 1 is necessary to track which grid elements constitute the domain's boundary ${}^{\bar{h}}\mathcal{T}^{\partial^{\bar{h}}\bar{\omega}}$. To read this algorithm, it is necessary also to introduce the set of inactive elements ${}^{\bar{h}}\mathcal{T}^{in}$, defined as ${}^{\bar{h}}\mathcal{T}^{in} := {}^{\bar{h}}\mathcal{T} \setminus {}^{\bar{h}}\mathcal{T}^{act}$. Among the facets belonging to the

set of boundary elements ${}^{\bar{h}}\mathcal{T}^{\partial^{\bar{h}}\bar{\omega}}$, Algorithm 2 selects those satisfying one of the following criteria:

- the facet is shared between one boundary element and one active non-boundary element; or

- the facet is between two adjacent boundary elements.

While selecting the former set of facets (criterion at the first bullet point) is justified by prolonging the coercivity from the bulk of the material, the latter (criterion at the second bullet point) is mainly required for boundary corner elements not directly connected to an active non-boundary element. The union of the selected facets, that is,

$$ {}^{\bar{h}}\gamma^F = \bigcup_{F \in \mathscr{F}} F \quad (44) $$

constitutes the surface ${}^{\bar{h}}\gamma^F$ necessary for Equation (43). Unlike the volume integrals in Equation (42), Equation (43) is integrated via the Gauss-Legendre quadrature rule using Gauss points seeded on the grid.

Algorithms 1 and 2 (as well as Equation (43)) are relevant to sMPM and GIMPM shape functions. Unlike the unfitted FEM,

---

ALGORITHM 1 | Selection of the boundary elements belonging to ${}^{\bar{h}}\mathcal{T}^{\partial^{\bar{h}}\bar{\omega}}$.

```
ʰ𝒯^∂ʰω̄ ← []
el_count ← 1
foreach element T ∈ ʰ𝒯^act do                          // loop over active elements
   face_count ← 1
     foreach facet F ∈ clos(T) do                      // loop over facets of the selected active element
        if F ∈ clos(ʰ𝒯^in) then                        // check if facet is also shared with an inactive element
         | Add T to ʰ𝒯^∂ʰω̄;
        end
        face_count ++
     end
   el_count ++
end
```

ALGORITHM 2 | Selection of the facets for the face ghost penalty.

```
𝓕 ← []
el_count ← 1
foreach element Tᵢ ∈ ʰ𝒯^∂ʰω̄ do                         // loop over boundary elements
   face_count ← 1
     foreach facet F ∈ clos(Tᵢ) do                     // loop over facets of the selected boundary element
        if F ∈ clos(ʰ𝒯^∂ʰω̄ \ Tᵢ) then                  // check if facet is shared with another boundary element
         | Add F to 𝓕;
        end
        if F ∈ clos(ʰ𝒯^act \ ʰ𝒯^∂ʰω̄) then              // check if facet is shared with active non-boundary element
         | Add F to 𝓕;
        end
        face_count ++
     end
   el_count ++
end
```

---

in which the boundary elements constitute a single layer of elements, high-order MPMs can contain multiple layers of boundary elements due to the stencil of these high-order shape functions, which cover multiple elements simultaneously. This situation can also occur for the GIMPM. However, since only two layers of boundary elements can be active simultaneously in the worst-case scenario for the GIMPM, Algorithms 1 and 2 prove to be sufficient (see Examples 5.2 and 5.4).

As stabilising multiple layers can be quite burdensome, Yamaguchi et al. [54] adapted the Extended B-splines (EBS, see Höllig et al. [55, 56]) technique to stabilise MPM formulations employing B-spline shape functions. Another interesting technique has been proposed by Badia et al. [57] for the unfitted FEM, which aggregates elements on the boundary suffering from the small-cut issue. However, these techniques can be problematic to integrate into the current framework: on the one hand, the EBS-MPM cannot be used for the considered low-order shape functions, while aggregating can be particularly difficult, especially in light of the inf-sup stable overlapping meshes adopted in this manuscript. These are explained in the following section.

4.4 | Qk_{SD}-Qk Spatial Discretisation

To comply with the inf-sup requirement, the concept of Qk_{SD}-Qk elements from the FEM is here adapted to the MPM. This is achieved by overlapping a coarser grid for the pressure field (of length h) on a finer mesh for the displacement field (of length $h/2$)[7]. For simplicity, both these meshes are Cartesian.

Qk_{SD}-Qk elements are well-acknowledged in the FEM (see, for instance, Dortdivanlioglu et al. [44] for a $u - p^f$ formulation), and the idea can be traced at least back to Bercovier and Pironneau [58], who gave the first error estimate for two- and three-dimensional FEM of these kinds of elements. In the case of an MPM formulation, to the best of the authors' knowledge, the Qk_{SD}-Qk concept has been applied only to problems involving incompressible elasticity and with B-spline shape functions [59].

Using Qk_{SD}-Qk elements implies that the finite-dimensional spaces (37) and (38) for the trial functions become

$$^{h/2}\mathscr{V}_{\overline{u}} = \left\{ ^{h/2}u \in \left[C^m\left(^{h/2}\overline{\omega} \right) \right]^{n^{dim}} \middle| ^{h/2}u(x) = N_a^{h/2}(x)u_a \right.$$
$$\left. \text{with } a \in \text{clos}\left(^{h/2}\mathcal{T}^{act} \right), \, ^{h/2}u = \overline{u} \text{ on } ^{h/2}\overline{\gamma}^{\overline{u}} \right\} \quad (45)$$

$$^{h}\mathscr{W}_{\overline{p}} = \left\{ ^{h}p^{(f)} \in C^m\left(^{h}\overline{\omega} \right) \middle| ^{h}p^{(f)}(x) = N_a^h(x)\,p_a \text{ with } a \in \text{clos}\left(^{h}\mathcal{T}^{act} \right) \right\} \quad (46)$$

and similar definitions follow for the spaces of test functions $^{h/2}\mathscr{V}_{\mathbf{0}}$ and $^{h}\mathscr{W}_{\mathbf{0}}$. Using Qk_{SD}-Qk-inspired meshes and including the face ghost stabilisation Equation (43), the weak form becomes: find $^{h/2}u \in {}^{h/2}\mathscr{V}_{\overline{u}}$ and $^{h}p^{(f)} \in {}^{h}\mathscr{W}_{\overline{p}}$ such that, for $t \in [0, \tilde{t}]$,

$$\int_{MP_\omega} \delta\mathbf{w}_a \, \mathbf{grad}\left(N_a^{h/2} \right) : \left(\sigma' - N_b^h \, p_b \, \mathbf{1} \right) dv$$
$$- \int_{MP_\omega} \left(\delta\mathbf{w}_a \, N_a^{h/2} \right) \cdot \rho\mathbf{b} \, dv - \int_{\gamma^{\bar{t}}} \left(\delta\mathbf{w}_a \, N_a^{h/2} \right) \cdot \bar{t} \, da$$
$$+ \gamma^A \, \frac{h}{2} \int_{h/2 \gamma F} \delta\mathbf{w}_a \left[\left(\mathbf{grad}\left(N_a^{h/2} \right) \cdot \mathbf{n} \right) \right] \cdot \left[\left(\mathbf{grad}\left(N_b^{h/2} \right) \cdot \mathbf{n} \right) \right] \mathbf{u}_b \, da = 0,$$
$$\forall \delta\mathbf{w}_a \in {}^{h/2}\mathscr{V}_{\mathbf{0}} \quad (47)$$

$$\int_{MP_\omega} \left(\delta\eta_a \, N_a^h \right) \rho_0^{(f)} \frac{\dot{j}}{J} \, dv + \int_{MP_\omega} \frac{\kappa}{g} \, \delta\eta_a \, \mathbf{grad}\left(N_a^h \right) \cdot \left(\mathbf{grad}\left(N_b^h \right) p_b - \rho_0^{(f)} \mathbf{b} \right) dv$$
$$- \int_{\gamma^{\overline{q}}} \left(\delta\eta_a \, N_a^h \right) \overline{q} \, da + \gamma^{pen} \int_{\gamma^{\overline{p}}} \left(\delta\eta_a \, N_a^h \right) \left(N_b^h \, p_b - \overline{p} \right) da$$
$$+ \gamma^C h \int_{h_\gamma F} \delta\eta_a \left[\left(\mathbf{grad}(N_a^h) \cdot \mathbf{n} \right) \right] \left[\left(\mathbf{grad}(N_b^h) \cdot \mathbf{n} \right) \right] p_b \, da = 0$$
$$\forall \delta\eta_a \in {}^h\mathscr{W}_0 \quad (48)$$

giving the initial condition $^{h/2}u(t = 0) = u_0$. In the above equations, γ^A and γ^C are the coefficients used to the scale the effect of the ghost penalty terms and to match the physical units of the equations. For this latter purpose, the units of γ^A must be similar to a stress measure, while the units of γ^C should be the same as those of the κ/g.

Figure 2a shows the application of the face ghost stabilisation to the finer mesh of length $h/2$ for the displacement field (i.e., ghost penalty term added to Equation (47)), distinguishing between inactive and active elements, boundary elements, and boundary facets. Similarly, Figure 2b illustrates the same quantities for the coarser mesh of length h employed for the pressure field (i.e., the ghost penalty term added to Equation (48)). The combined result of the different stabilised surfaces for the displacement and pressure fields is represented in Figure 2c.

Equations (47) and (48) represent a stable scheme for implicit low-order $u - p^{(f)}$ formulation, which is inf-sup stable by design (as required by submatrix $\mathbf{B}$) and guarantees a solution thanks to submatrices $\mathbf{A}$ and $\mathbf{C}$ coercivity.

For the sake of completeness, it must be acknowledged that a plethora of inf-sup stabilised elements exist in the literature, and covering the complete literature on this subject is beyond the scope of this work. As for the FEM, the reader can refer to, for instance, Leborgne [60] for a recent publication discussing the inf-sup condition for different mixed formulations (and possible remedies) or to the monograph of Boffi et al. [45] for a complete discussion. The nature of Qk_{SD}-Qk elements makes its adaptation straightforward to use in the MPM, especially if low-order shape functions are used. On top of this, stable elements by design possess the advantage of not adding terms to the primary equations. This is particularly advantageous if the NR method is employed to solve the implicit primary equations, since fewer terms can be considered in the Jacobian matrix. In the following section, Qk_{SD}-Qk meshes are diversified for the sMPM and the GIMPM, and their inf-sup stability is investigated.

4.4.1 | sMPM Shape Functions

Having selected a Cartesian mesh composed of quadrilateral (or hexahedral, if $n^{dim} = 3$) elements, the basis functions are constructed using the tensor product of one-dimensional functions. In the case of sMPM for the generic mesh of length $\tilde{h}$, first-order Lagrange polynomials are employed, that is,

$$N_a^{\tilde{h},1}(\xi) = \begin{cases} 1 + \xi/\tilde{h}, & \text{if } -\tilde{h} < \xi \leq 0 \\ 1 - \xi/\tilde{h}, & \text{if } 0 < \xi \leq \tilde{h} \end{cases} \quad (49)$$

where $\xi = {}^{mp}x - {}^{\tilde{h}}x_a$ denotes the one-dimensional local coordinate computed as the difference between the material point's coordinate and the grid nodal coordinate. The use of these shape
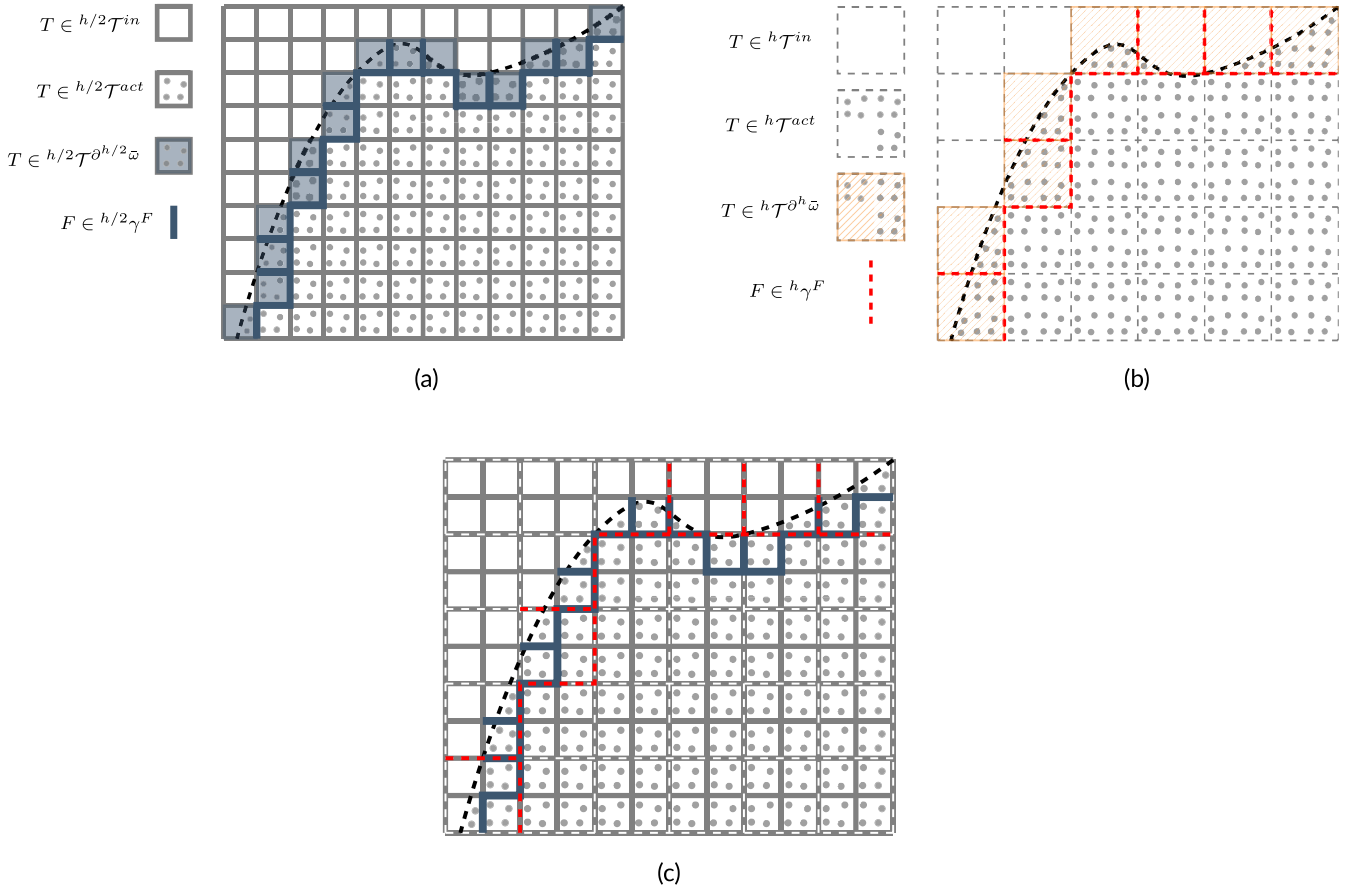
$$T \in {}^{h/2}\mathcal{T}^{in}$$
$$T \in {}^{h/2}\mathcal{T}^{act}$$
$$T \in {}^{h/2}\mathcal{T}^{\partial^{h/2}\bar{\omega}}$$
$$F \in {}^{h/2}\gamma^{F}$$

(a)

$$T \in {}^{h}\mathcal{T}^{in}$$
$$T \in {}^{h}\mathcal{T}^{act}$$
$$T \in {}^{h}\mathcal{T}^{\partial^{h}\bar{\omega}}$$
$$F \in {}^{h}\gamma^{F}$$

(b)

(c)

FIGURE 2 | Algorithmic selection of boundary elements and facets (top row) for finer (left) and coarser (right) meshes, and stabilised facets (bottom row). (a) Application of Algorithms 1 and 2 to the finer mesh for ${}^{h/2}\boldsymbol{u}$. (b) Application of Algorithms 1 and 2 to the coarser mesh for ${}^{h}p^{(f)}$. (c) Final result of facets where face ghost stabilisations are applied.

functions for a Q1$_{SD}$-Q1 FEM $\boldsymbol{u} - p^{(f)}$ formulation has been tested in Dortdivanlioglu et al. [44], employing the patch test proposed by Chapelle and Bathe [47] for mixed FEM formulations. Employing this result and given the similarities between the FEM and the MPM, it can be concluded that Q1$_{SD}$-Q1 mesh-based solutions for sMPM discretisation inherit inf-sup stability from their FEM counterpart. This conclusion is also substantiated by Example 5.1.

4.4.2 | GIMPM Shape Functions

The GIMPM shape functions in 1D are obtained via the convolution of a constant function denoting the length of the particle $2l_p$ (named the *characteristic function*) with the sMPM shape function given by Equation (49). The reader is referred to Bardenhagen et al. [32] or Charlton et al. [33] for this convolution integral procedure. The one-dimensional GIMPM shape functions defined on a mesh of length $\tilde{h}$ are given by

$$S_a^{\tilde{h}}(\xi) = \begin{cases} (\tilde{h} + l_p + \xi)^2/(4\tilde{h}l_p), & \text{if} \quad -\tilde{h} - l_p < \xi \leq -\tilde{h} + l_p \\ 1 + \xi/\tilde{h}, & \text{if} \quad -\tilde{h} + l_p < \xi \leq -l_p \\ 1 - \xi^2/(2\tilde{h}l_p) - l_p^2/(2\tilde{h}l_p), & \text{if} \quad -l_p < \xi \leq l_p \\ 1 - \xi/\tilde{h}, & \text{if} \quad l_p < \xi \leq \tilde{h} - l_p \\ (\tilde{h} + l_p - \xi)^2/(4\tilde{h}l_p), & \text{if} \quad \tilde{h} - l_p < \xi \leq \tilde{h} + l_p \end{cases} \quad (50)$$

with $\xi = {}^{mp}x - {}^{\tilde{h}}x_a$ as above.

Figure 3 shows that three combinations of the polynomials are locally available when using the GIMPM shape functions for Qk$_{SD}$-Qk meshes: Q2$_{SD}$-Q2, Q1$_{SD}$-Q1, and Q2$_{SD}$-Q1. As for the case of linear polynomials in Section 4.4.1, these elements have been separately tested by Dortdivanlioglu et al. [44] for the FEM using the patch test in Chapelle and Bathe [47]. When examined independently, each of these elements has been shown to be inf-sup stable. While it is not possible to apply this test directly to an MPM formulation (patch tests cannot be adapted to the MPM), a thought experiment can be built by employing shape functions in Equation (50) to construct an FEM discretisation and using the results from Dortdivanlioglu et al. [44]. The test proposed by Bathe and Chapelle [47] checks an eigenvalue-eigenvector problem using matrices relative to discrete bilinear forms. This test is repeated for different decreasing mesh sizes, and it is considered as passed when the minimum eigenvalue does not decrease with finer grids. The same matrices for the eigenvalue-eigenvector problem employing shape functions in Equation (50) are a linear combination of the above elements. This holds since each integration point singularly contributes as Q2$_{SD}$-Q2 or Q1$_{SD}$-Q1 or Q2$_{SD}$-Q1 to its element, and the assembling process sums each integration point's contribution. Hence, the boundedness of the minimum eigenvalue resulting from this FEM-like discretisation using shape functions in Equation (50) follows since it is linear algebra (eigenvalue problem) applied to matrices of bilinear forms.
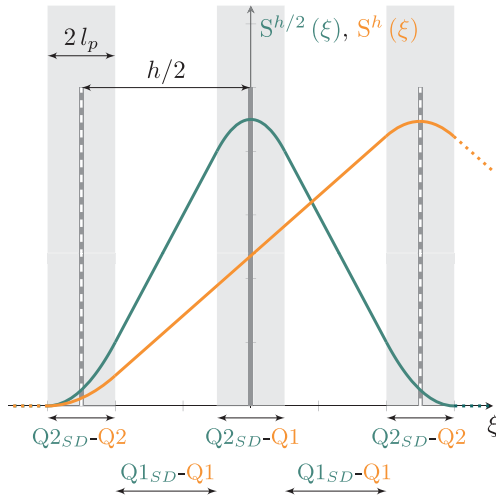
FIGURE 3 | Combination of GIMPM functions on overlapping meshes. Thick grey lines illustrate the finer mesh, while white dashed lines represent the coarser one.

This rationale is confirmed by numerical Examples 5.3 and 5.4, which adopt GIMPM shape functions and exhibit stable pressure values.

4.5 | Time Discretisation

In addition to the spatial discretisation introduced above, a temporal discretisation is required and this work considers the following implicit Backward-Euler time integration relative to the divergence of the velocity field

$$\mathbf{div} \cdot \boldsymbol{v} = \frac{\dot{J}}{J} = (\ln J)^{\cdot} \approx \frac{(\ln J_{n+1} - \ln J_n)}{\Delta t} \qquad (51)$$

where the subscript $n+1$ denotes the current time step and n the previous one.

The literature (see, for instance, Sun et al. [61] or Zhao and Choo [22]) recognises the role played by the above time discretisation to avoid negative values of the Jacobian. However, the current formulation considering an incompressible solid phase imposes a more severe constraint on the Jacobian than $J > 0$. This can be quickly verified if inequalities (3) relative to the Eulerian porosity are substituted in solid mass conservation Equation (8). The reader can refer to Pretti et al. [42] for further details and consequences of the above inequalities. Despite this consideration, the above formula possesses another desirable feature for the MPM, discussed below in Section 4.6, and it is thus employed.

4.6 | Mapping Processes and MPs' Domain Update

As mentioned in Section 4.1, two mapping processes take place in an MPM step. The Point-to-Grid (P2G) mapping (phase (ii) in Figure 1) initialises the nodal grid unknowns, transferring the information from the MPs. This mapping process is required to conserve physical properties of interest relative to the mapped information. In the context of the dynamics of a solid body, for instance, the velocity mapped from the MPs to the grid is expected to conserve, as much as possible, momenta (linear and angular) and kinetic energy to avoid numerical dissipation (see Love and Sulsky [62] or Pretti et al. [63]). A similar rigorous procedure should be expected for a poro-mechanical problem. However, mapping the velocity can be avoided for a quasi-static problem using Equation (51), since the Jacobian J is not required on the grid for computational purposes. As for the other primary variable, the fluid pressure relates to a form of energy stored in the fluid body only if the considered material is compressible, as pointed out by Miehe et al. [43]. Owing to Assumption 6, this work considers an incompressible fluid constituent, which is not required to be mapped as the pressure acts as a Lagrange multiplier, which does not entail any form of energy. Overall, it emerges that G2P mapping is not required in this context, that is, quasi-static simulations considering an incompressible fluid phase. However, this procedure can take place for estimating better predictors for the NR scheme, but these estimates are free from consideration of numerical dissipation.

Once the grid solution is achieved, this must be mapped to the MPs before grid disposal (phase (v) in Figure 1). Unlike the P2G mapping, the Grid-2-Point (G2P) mapping must always take place, as it is the MPs' role to store information necessary to run the analysis through different steps. Under the same assumptions considered in the above paragraph for the P2G mapping (i.e., quasi-static simulations involving an incompressible fluid), the G2P mapping is not required to conserve physical quantities of interest for the same reasons outlined above. Hence, the shape functions can be straightforwardly used to map the values of the unknowns from the grid nodes to the MPs, that is,

$$^{mp}\boldsymbol{u}_{n+1} = {}^{mp}\boldsymbol{u}_n + \mathrm{N}_a^{h/2}\left({}^{mp}\boldsymbol{x}_{n+1}\right)\Delta\mathbf{u}_a \qquad (52)$$

$$^{mp}p_{n+1} = \mathrm{N}_a^h\left({}^{mp}\boldsymbol{x}_{n+1}\right)\left(\mathrm{p}_{n+1}\right)_a \qquad (53)$$

where $\Delta\mathbf{u}_a$ is the difference in the time step of the grid displacements, that is, $\Delta(\bullet) := (\bullet)_{n+1} - (\bullet)_n$. The above updates exploit the considerations drawn so far: on the one hand, the initial displacement on the grid $\left(\mathbf{u}_a\right)_n$ is not reconstructed with the P2G mapping (the unknown of the system of primary equations can directly be $\Delta\mathbf{u}_a$); on the other, the pressure field can be re-written both at the MP and grid levels because it is not related to an energy measure.

While the update of the mixed volume for the sMPM follows the standard procedure for volume update using the Jacobian, the length of the characteristic function for the GIMPM requires an update that can differ for the different Cartesian directions. This work follows the *corner update procedure* proposed by Coombs et al. [36]. The reader is referred to this reference for further details on its implementation and the exhibited advantages over the other techniques.

5 | Numerical Examples

The model detailed in Section 2, formulated in a weak sense in Section 3, and discretised in Section 4, is below investigated via four different examples, each exploring a particular feature

of the proposed formulation. The implementation of the outlined model has been carried out in an extended version of AMPLE [64].

5.1 | Terzaghi Mono-Dimensional Consolidation

Example Scope

The numerical investigation provided by the Terzaghi mono-dimensional consolidation (see Figure 4 and, for comparison, [65]) delivers a two-fold goal. A comparison considering two meshes is made between the Qk_{SD}-Qk meshes (specifically using sMPM, that is, $Q1_{SD}$-$Q1$) and the Polynomial Pressure Projection (PPP) with a single mesh. The PPP is one of the most widely adopted stabilisation techniques in the literature for $u - p^{(f)}$ (see White and Borja [66] for the FEM and Zhao and Choo [22] for its adaptation to the MPM). The results on the two meshes are compared near zero consolidation time versus an established critical time for $u - p^{(f)}$ formulations (see Vermeer [67]). This critical time states that the coarser simulation shows oscillating pressure, while the finer analysis does not. While the simulations with $Q1_{SD}$-$Q1$ meshes agree with these predictions, it is shown that the analyses employing the PPP exhibit pressure instability for both meshes. Furthermore, in the case of the coarser unstable simulation, it is investigated how this instability dissipates over time for the simulation using $Q1_{SD}$-$Q1$ meshes.

The analytical values of pressure are well-known in the small-strain regime and are given by (see, for instance, [65])

$$P(Z,T) = \sum_{m=0}^{\infty} \frac{2}{M} \sin(MZ) \exp(-M^2 T)$$
$$\text{with } M = \frac{\pi}{2}(2m+1) \quad \text{and } m = 0, 1, \cdots \in \mathbb{N}_0 \quad (54)$$

where the adimensional quantities in the above equation are defined as follows

$$P := \frac{p^{(f)}}{w}; \qquad Z := \frac{z}{H}; \qquad T := \frac{c_v}{H^2} t \quad (55)$$
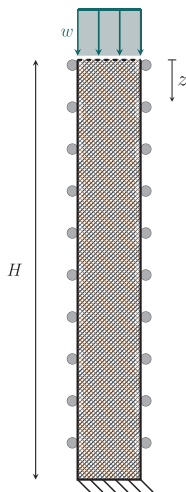

FIGURE 4 | Illustration of the Terzaghi mono-dimensional problem. Permeable surfaces are designed by the dashed line.

with w being the magnitude of the overburden and H the height of the column. The relationship between the coefficient of consolidation c_v and other hydro-mechanical parameters is given by

$$c_v = \frac{\left(\frac{K}{n_0} + \frac{4}{3}G\right)}{\rho_0^{(f)} g} \kappa \quad (56)$$

where $\frac{K}{n_0}$ is the initial tangent modulus of the improved Hencky material described by Equation (15).

Setup

The hydro-mechanical parameters are the same as those employed by Zhao and Choo [22] and are reported in Table 1. Owing to the assumed parameters, it is expected that the numerical values, computed in the finite strain context, can reproduce the analytical results set in the small strain theory. Two MPs per direction are initially positioned for each element of the finer mesh. Owing to this initial discretisation and given that small displacements are expected, the small-cut issue detailed in Section 4.2 does not occur in this example. Thus, the ghost stabilisation included in Equations (47) and (48) are not considered for this problem.

As mentioned above, two different vertical discretisations have been considered, and the initial selected time step is $t_0 = 0.1$ s. These discretisations have been designed to comply with (in the case of $n_y^{\text{els}} = 320$) and violate (in the case of $n_y^{\text{els}} = 160$) at the first time step the time value prescribed by Vermeer and Verruijt [67] for implicit $u - p^{(f)}$ formulations, this being

$$t \geq \frac{\Delta h_y^2}{6 \, c_v} \begin{cases} \approx 0.09 \text{ s} & \text{if } n_y^{\text{els}} = 320 \\ \approx 0.36 \text{ s} & \text{if } n_y^{\text{els}} = 160 \end{cases} \quad (57)$$

To avoid unnecessary computational time and still provide a good description of the consolidation phenomenon, the time-step partition observes the geometric series to complete the consolidation process (i.e., $T = 1$)

$$\sum_{p=0}^{n-1} c^p t_0 \approx \frac{H^2}{c_v} \quad (58)$$

where the common ratio $c = 1.01673$ has been selected to run the simulation in $n = 550$ time-steps.

TABLE 1 | Summary of the parameters considered in the analysis of the Terzaghi mono-dimensional consolidation.

Parameter settings		
Material parameters	$\frac{K}{n_0}$, G	1×10^6 Pa, 6×10^5 Pa
	κ_0	10^{-7} m s^{-1}
	$\rho_0^{(f)}$	1000 kg/m^3
Geometry and loading	H	1 m
	w	100 kPa

The analyses have been run using sMPM shape functions (Q1$_{SD}$-Q1 meshes). However, given that small displacements are expected, no appreciable difference could be noticed if the GIMPM shape function should have been employed.

The parameter for the PPP vector is $\frac{1}{2G}$, which is widely adopted in the literature (see Zhao and Choo [22] and references therein).

Results Discussion

From a comparison between Figures 5a and 5b, it is clear that the formulation proposed in this paper (green line) agrees with the prediction of unstable (Figure 5a) and stable (Figure 5b) time provided by Equation (57). Conversely, the PPP (red line) exhibits unstable behaviour even for the predicted stable discretisation with $n_y^{els} = 320$. Moreover, it can be seen that the instability caused by the PPP propagates through more vertical elements than its Q1$_{SD}$-Q1 counterpart for both situations. It must be observed that these results comply with the literature: Preisig and Prevost [29] stated that the PPP is unable to remove pressure oscillation near the draining boundary, and Monforte et al. [68], adopting a $u - w - p^{(f)}$ formulation, showed pressure oscillating behaviour for a high-frequency wave propagation problem. These studies confirm that the PPP was not designed to stabilise poromechanical problems in which the pressure field belongs to $H^1(\omega)$: the original application of the PPP (see Dohrmann and Bochev [69]) was Stokes problems, which requires the pressure field to be $H^0(\omega)$. The peaks shown in Figures 5a and 5b (and confirmed by the literature) correspond with sharp pressure gradients (i.e., with the phenomenon progressively passing from undrained to drained), which the PPP was not designed to stabilise.

Figure 6 (particularly its magnification) investigates the persistence of the spurious peak for the Q1$_{SD}$-Q1 formulation in the unstable case (i.e., $n_y^{els} = 160$). The numerical results agree with Equation (57), which prescribes a stable time bigger than ≈ 0.36 s. For the adimensional time $T \approx 1.33 \cdot 10^{-5}$ (corresponding to ≈ 0.74 s), the peak is practically extinguished. Its pressure value is 2.14% bigger than its analytical one, which is significantly lower than the one exhibited in Figure 5a for $T \approx 1.8 \cdot 10^{-6}$ (corresponding to ≈ 0.1 s), this being 17.5% bigger compared to the analytical value. For the $T \approx 1.05 \cdot 10^{-4}$ (corresponding to ≈ 5.83 s), there is no appreciable difference between the numerical and the analytical solution. This overlap between the numerical investigation and the analytical solution for the excess pore pressure isochrones continues for the rest of the simulation, until consolidation has entirely taken place.

5.2 | Investigation of the Face Ghost Penalty

Example Scope

While the previous example focused on the stabilising effect given by Q1$_{SD}$-Q1 elements, this numerical exercise (illustrated in Figure 7) is particularly aimed at investigating the beneficial role of ghost penalties when applied to the matrices **A** and **C** appearing in the Jacobian matrix. If adopting (as is the case in this example) Qk$_{SD}$-Qk meshes, the drained case requires coercivity of both these bilinear forms associated with the above matrices to guarantee solvability.

The effectiveness of the face ghost stabilisation applied to Equations (47) and (48) is investigated for different values of the parameters γ^A and γ^C. The spanned values of these parameters have been chosen to be not too small, resulting in insignificant effects, nor too high, leading to potential locking phenomena (see Badia et al. [70]). This example bears similarities with other numerical tests proposed by Coombs [30] in the MPM context and by Kothari and Krause [71] and Sticko et al. [72] for the unfitted FEM.
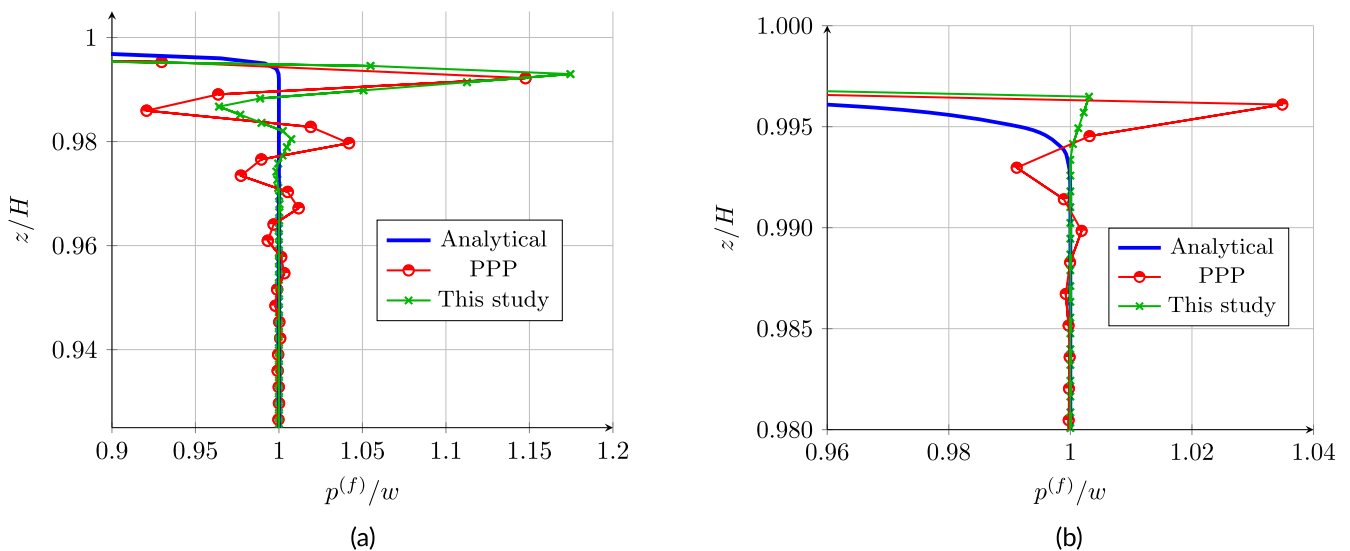

FIGURE 5 | Graphical comparison between analytical formula and numerical solutions obtained with the PPP stabilisation and Q1$_{SD}$-Q1 meshes. (a) Excess pore pressure isochrones comparison at the time $T \approx 1.8 \times 10^{-6}$ s for the case with $n_y^{els} = 160$. (b) Excess pore pressure isochrones comparison at the time $T \approx 1.8 \times 10^{-6}$ s for the case with $n_y^{els} = 320$.

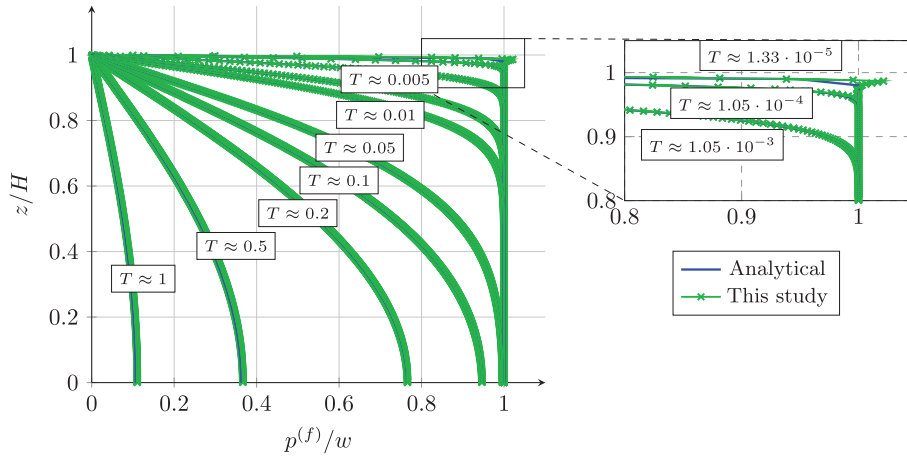**FIGURE 6** | Excess pore pressure isochrones for the case with $n_y^{\text{els}} = 160$.
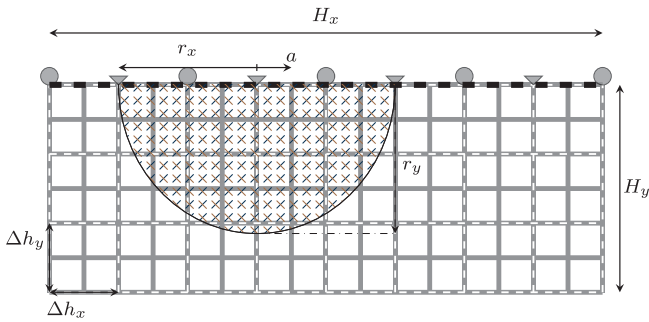

FIGURE 7 | Geometry and initial setup for the considered ellipse. Each initial setup consists of seeding the MPs discretising the ellipse in a different position, described by the coordinate a, while keeping the meshes (finer in grey, coarser dashed in white) fixed. New MP setups are generated for different values of a. Drained conditions are applied at the top of the mesh (dashed black line).

Setup

The half of an ellipse illustrated in Figure 7 is made of an ideal porous material, whose parameters are listed in Table 2. Since the scope of this investigation lies in the examination of the small-cut issue (and its remedy), the geometrical aspect, that is, the overlap between the physical domain and shape functions' stencil, is examined. This justifies two aspects: on the one hand, the assumption of ideal, non-descriptive, hydro-mechanical parameters; on the other, the use of a geometry such as an ellipse. This form combines a periodic behaviour along the coordinate a (see Figure 7) and aggravates the small-cut problem at the bottom limit of the ellipse.

Three MPs per direction are initially equally distributed for each element of the finer mesh. The MPs lying outside the analytical shape described by the half of the ellipse are then removed. This setup is repeated for different values of the coordinate a, which is varied progressively for each simulation. For each of these discretisations, the submatrices **A** and **C** in the Jacobian are assembled so that the effect of the ghost stabilisation can be assessed for different physical MP-based domain-mesh interactions.

TABLE 2 | Summary of the parameters considered in the investigation of the ghost penalty example.

Parameter settings		
Material Parameters	$\dfrac{K}{n_0}$, G	1 Pa, 1 Pa
	κ_0	1 m s^{-1}
	$\rho_0^{(f)}$	1 kg/m^3
Geometry	H_x, H_y	8 m, 3 m
	r_x, r_y	2 m, 2.15 m
Grid	Δh_x, Δh_y	1 m, 1 m

It must be noted that, for the sMPM, it is not possible to assign an element to an MP when this lies precisely on an element boundary. Since this occurs for the finer mesh when $a = \frac{\Delta h_x}{4} * p$, with $p = 1, 2, \cdots \in \mathbb{N}$, these sampling locations are avoided for the sMPM. This choice explains the rupture of periodic behaviour, which is particularly evident in Figure 8a. Nonetheless, it must be underlined that this situation is due to the specificity of the setup and is highly unlikely to occur in standard simulations.

Results Discussion

As it can be appreciated from Figure 8, there is considerable difference in the condition numbers (denoted by $\kappa(\bullet)$, with $(\bullet)$ being the considered submatrix) for unstabilised sMPM and GIMPM, with the latter showing on average three orders of magnitude higher condition number for the same setup. This behaviour is due to the shape functions stencil, which is more extended for the GIMPM.

Figure 8a highlights how the lowest value of ghost penalty ($\gamma^A = E \cdot 10^{-4}$) does not contribute significantly to the submatrix **A** condition number in the case of sMPM. Diversely, in the case of the GIMPM in Figure 8c, the effect of the ghost penalty for $\gamma^A = E \cdot 10^{-4}$ reduces the peak values by approximately an order of magnitude, even though the general pattern follows similarly that of the unstabilised version. These peaks are more levelled for the case of $\gamma^A = E \cdot 10^{-2}$ and entirely smoothed for the case of $\gamma^A = E$, which exhibits condition numbers approximately 4.5
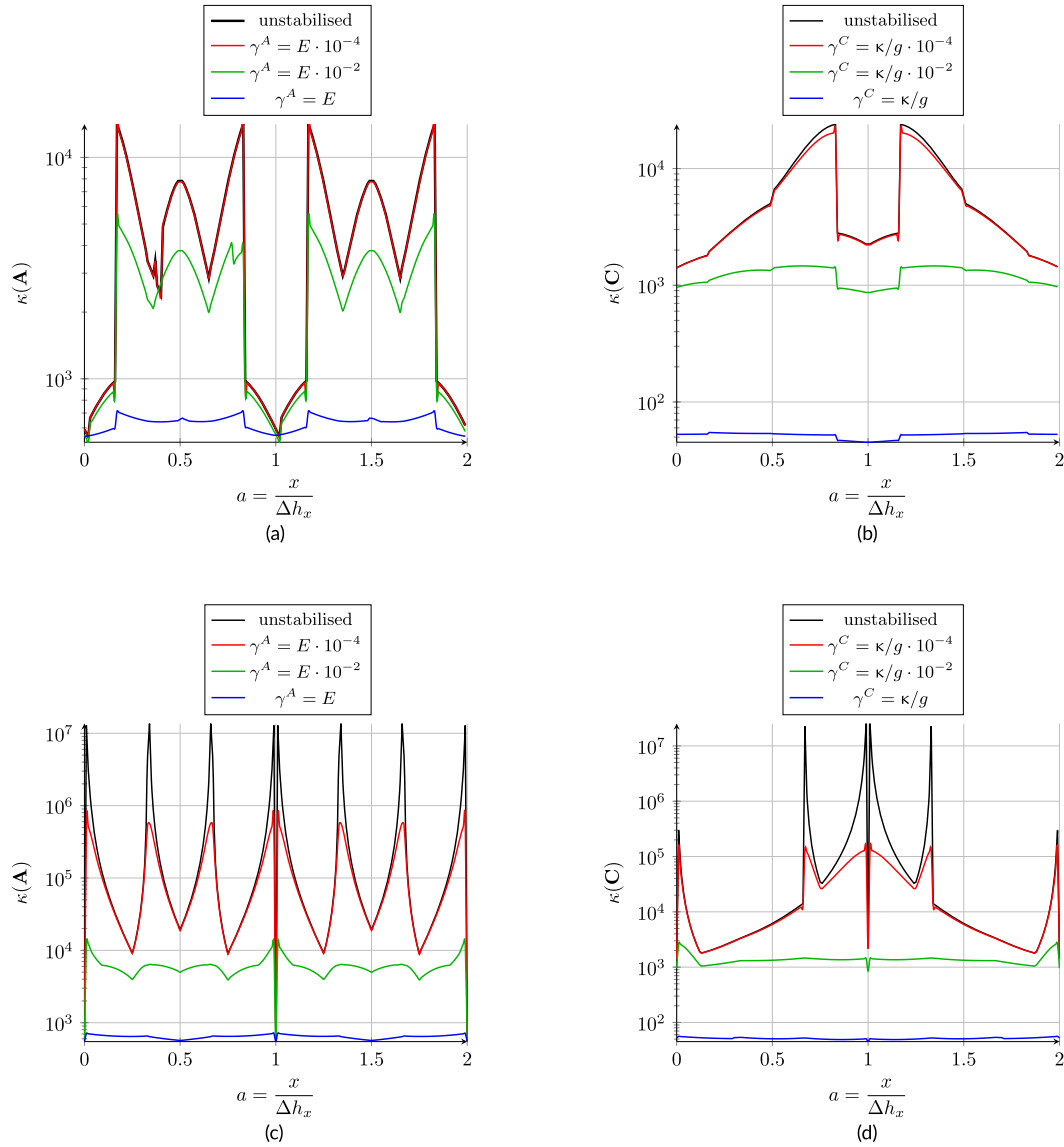
FIGURE 8 | Effects of the applied ghost penalty parameters on the condition number of submatrices **A** (left column) and **C** (right column) in the case of sMPM (top row) and GIMPM. (bottom row). (a) Condition numbers for the **A** sub-matrix for translating domains, sMPM. (b) Condition numbers for the **C** sub-matrix for translating domains, sMPM. (c) Condition numbers for the **A** sub-matrix for translating domains, GIMPM. (d) Condition numbers for the **C** sub-matrix for translating domains, GIMPM.

orders of magnitude lower than the peaks of the unstabilised version. Back to Figure 8a for the sMPM, it can be seen how $\gamma^A = E$ leads to overall smooth behaviour, with the condition number being approximately 1.5 orders of magnitude below the unstabilised peaks. The value $\gamma^A = E \cdot 10^{-2}$ contributes less significantly to stabilising the sMPM than its GIMPM counterpart. Similar trends can be seen for the condition number of the submatrix **C** in the case of sMPM (Figure 8b) and GIMPM (Figure 8d).

Owing to the previously mentioned lack of rigorous analysis for the MPM, the condition numbers of the submatrices **A** and **C**, even if they benefit from the ghost stabilisation, are still dependent to some degree on the intersection between the shape functions' stencil and the MP-based physical domain. This aspect diversifies the MPM from the unfitted FEM, where, once stabilised, the domain's cuts do not play a role in the condition number (as proved in Burman [51] and numerically demonstrated in

Kothari and Krause [71]). This difference amplifies the importance of carefully choosing the correct value of the stabilisation parameter, as some selections, even though effective, might not give the desired limitation on the condition number.

5.3 | Flexible Strip Foundation

Example Scope

The scope of this numerical test is to support the rationale provided in Section 4.4.2 regarding the stability of the different combinations of polynomial functions employed by the GIMPM formulation with Qk_{SD}-Qk meshes. To demonstrate that the pressure field is free from oscillations, a flexible footing loading has been applied at the top of a fully saturated porous material in plane-strain conditions (see Figure 9). Elastic and the

15 of 24

elasto-plastic cases have been considered. Since the application of the loading causes the considered body to displace substantially, it is expected that all the combinations of polynomials that the GIMPM basis functions exhibit will be met through the analysis, even if not uniformly or simultaneously.

Setup

Hydro-mechanical parameters are reported in Table 3, and the considered elastic material shares similarities with the one presented in Armero [73] in a very similar example. The modified Cam clay $\alpha - \gamma$ yield surface proposed by Collins and Hilder [74] has been considered for the elasto-plastic case (see, for instance, [75] for implementation details).

To apply the non-conforming pressure BCs, a penalty value of $\gamma^{\mathrm{pen}} = 5 \cdot 10^6 / \kappa_0$ was employed, where the hydraulic conductivity appears at the denominator for a matter of consistency with the physical units. The load has been linearly increased from zero to the value shown in Table 3. The elastic case can complete the
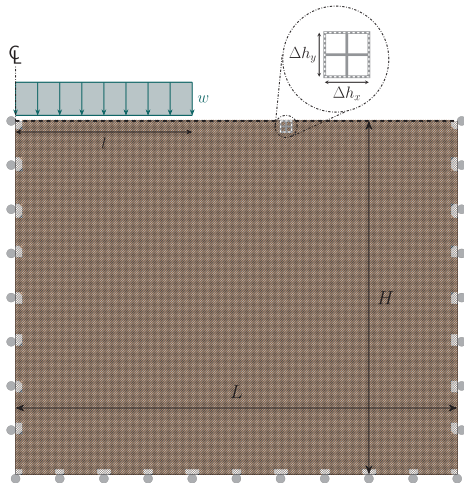
simulation in 20 time steps, while the plastic case reaches the limit load in correspondence with the 4th time step, where it is stopped.

Given the low number of MPs per element and the substantial displacements expected in this simulation, the ghost penalisation has been included. Based on the observations made in Example 5.2, the selected parameters for the penalty values are $\gamma^A = E \cdot 10^{-1}$ and $\gamma^C = \frac{\kappa_0}{g} \cdot 10^{-1}$.

Results Discussion

As can be seen from the contours shown throughout the analysis in Figure 10 for the elastic case, the fluid pressure does not present oscillations typical of violating the inf-sup condition. Even though showing spatially different distributions of pressure, these values are equally smooth for the final step of the elasto-plastic case shown in Figure 11b. As Figure 11a shows, plastic strains arise in correspondence with the footing angle, forming the expected wedge shape. This shape is also visible for the pressure field in Figure 11b, where the GIMPM Qk_{SD}-Qk meshes handle this horizontal gradient without interruptions or oscillations. Due to the continuity demonstrated for the different fields and situations in Figures 10 and 11, the chosen ghost parameters have proved suitable for stabilising the submatrices' conditioning number and achieving the continuous expected results.

Overall, the exhibited smooth values of pressure substantiate the explanation provided in Section 4.4.2 for the GIMPM shape functions, showing that these described Qk_{SD}-Qk stable meshes deliver oscillating-free solutions.

5.4 | Flexible Loading Applied to an Unconstrained Cube

Example Scope

The final example presented in this paper considers the three-dimensional flexible loading of an unconstrained cube, as illustrated in Figure 12, and compares the formulation proposed in this work, labelled (*a*), with formulation (*b*), which offers different characteristics. To be more specific,

- Simulation (*a*) includes the beneficial effects of the ghost stabilisations and the Qk_{SD}-Qk elements, as in Equations (47) and (48);

- Simulation (*b*) does not consider ghost stabilisations and employs equal-order interpolating functions over the same finer mesh.

For these specific simulations, the contribution to the stability of the Qk_{SD}-Qk elements and that of the ghost stabilisation mostly occur at two different stages. On the one hand, the presence of the overlapping grids avoids the pressure instability in nearly undrained conditions, when the material is mostly incapacitated to change its volume. On the other hand, the ghost stabilisation critically improves the condition number of the submatrices **A**
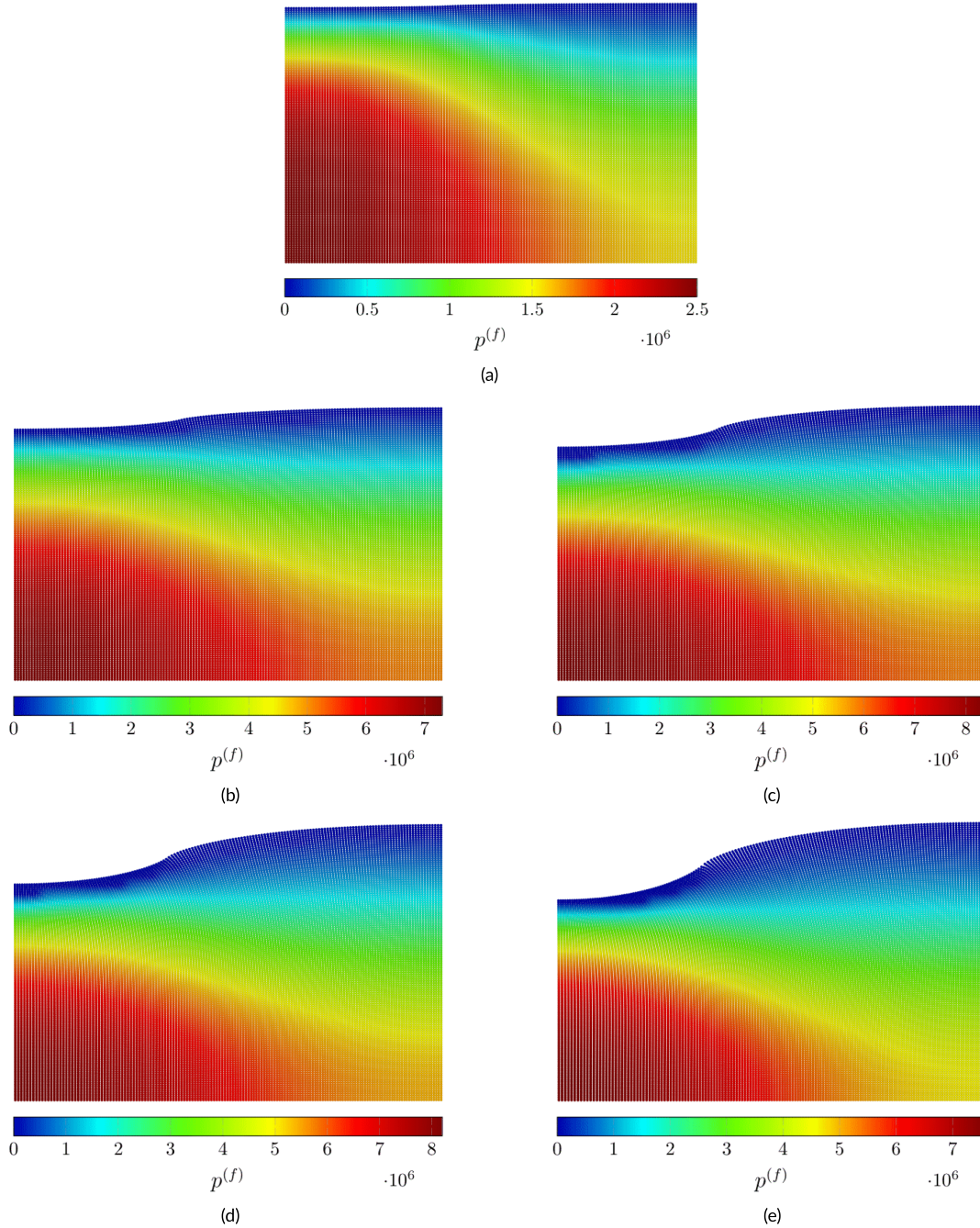

FIGURE 9 | Illustration of the flexible strip foundation problem. Permeable surfaces are designed by the dashed line.

TABLE 3 | Summary of the parameters considered in the analysis of the flexible strip foundation.

Parameter settings		
Material Parameters	K, G	1.062×10^8 Pa, 9.8×10^7 Pa
	α, γ, M, p_c	0.6, 0.9, 0.364, 7.5×10^7 Pa
	κ_0	$2.07 \cdot 10^{-3}$ m s^{-1}
	n_0	0.5
	$\rho_0^{(f)}$	1000 kg/m^3
Geometry and loading	L, H, l	20 m, 16 m, 8 m
	w	2.5×10^8 Pa
Time and time-step	T	10 s
	Δt	0.5 s
Grid and MPs	Δh_x, Δh_y	0.25 m, 0.25 m
	MPs per element (finer mesh)	4

FIGURE 10 | Contours of the pressure field across the simulation for the flexible footing loading, elastic case. (a) Contours of the fluid pressure field, 1st time step. (b) Contours of the fluid pressure field, 5th time step. (c) Contours of the fluid pressure field, 10th time step. (d) Contours of the fluid pressure field, 15th time-step. (e) Contours of the fluid pressure field, 20th time-step.

and **C** when the overlap between the shape functions' stencil and the background grid is minimal. Since the initial setup of these simulations considers conforming meshes, this small-cut situation occurs when the MPs move across the background mesh, that is, at a later stage of the simulation. Hence, the time-step segmentation of these when simulations has been designed to capture the initial nearly-undrained conditions (where Qk_{SD}-Qk elements can be appreciated) and, later on during the simulation, the large displacements taking place when the consolidation process kicks in significantly (and the ghost penalties are essential for a stable solution).

Setup

Figure 12 shows the initial setup of the problem, where roller boundary conditions are applied on the planes described by the equations $x = 0$, $y = 0$, and $z = 0$. Similarly to Example 5.3, zero atmospheric pressure is applied on the cube's external planes, using the corner penalty technique explained in Bird et al. [50] with a penalty factor $\gamma^{\text{pen}} = 2.2 \cdot 10^6/\kappa_0$. GIMPM shape functions are used for all of the analyses. The external load w is linearly increased from time 0 to time T of the simulation, ramping from 0 to the value reported in Table 4. The total time of the simulation
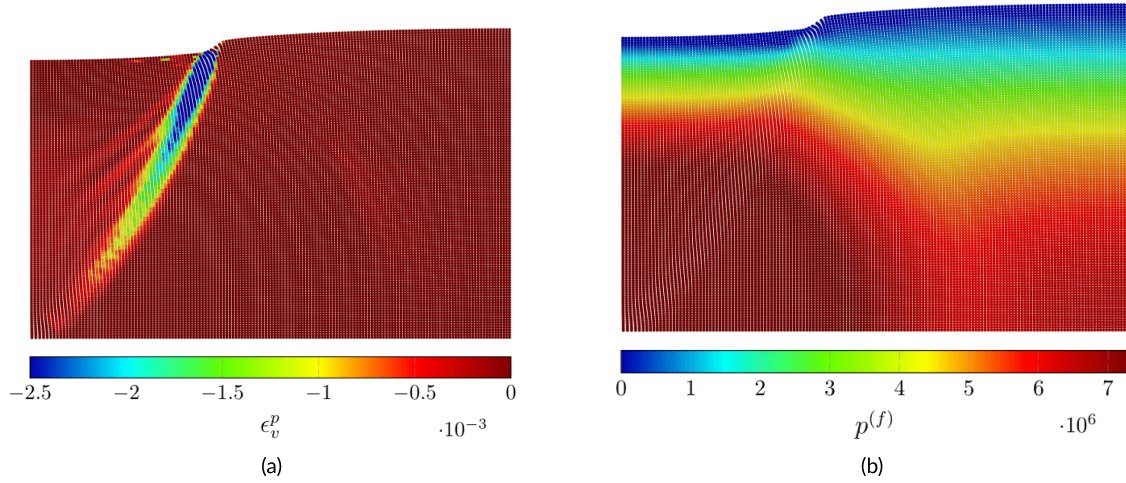
FIGURE 11 | Contours of different fields at the last time-step for the flexible footing loading, plastic case. (a) Contours of the plastic volumetric part of the logarithmic strain, last time-step. (b) Contours of the fluid pressure field, last time-step.
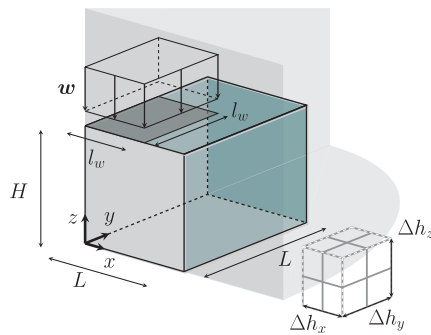

FIGURE 12 | Illustration of the flexible loading applied to an unconstrained cube. Rollers are applied on the grey-shaded surfaces, while zero atmospheric pressure is applied on the external surface of the slope, marked by the light blue colour. The load is applied on the top patterned area.

TABLE 4 | Summary of the parameters considered in the three-dimensional slope stability example.

Parameter settings		
Material Parameters	K, G	1.92×10^4 Pa, 9×10^4 Pa
	α, γ, M, p_c	0.6, 0.9, 0.364, 8×10^4 Pa
	κ_0	1×10^{-3} m s^{-1}
	n_0	0.2
Geometry and load	L, H	8 m, 6 m 6 m
	l_w	6 m
	$\|\boldsymbol{w}\| = w_z$	-8.52×10^3 Pa
Grid and MPs (coarser mesh)	$\Delta h_x = \Delta h_y = \Delta h_z$	0.167 m
	MPs per element	64

is $T \approx 657$ s. Time-step segmentation follows the geometric series given by the left-hand side of Equation (58), which is equal to the total time of the simulation T. This is achieved by setting $t_0 \approx 0.1206$ s and $c \approx 1.0234$, so that the simulation is run in 210 time steps. Table 4 reports the other parameters used in the simulations. The ghost penalty parameters used in Simulation (a) were $\gamma^A = E_0 \cdot 10^{-2}$ and $\gamma^C = \frac{\kappa_0}{g} \cdot 10^{-2}$.

Results Discussion

Figure 13 shows the mean condition number of the sub-matrices **A** (Figure 13a) and **C** (Figure 13b), from the 150th to the 210th time-step. The preceding steps are not considered in the graphs since the MPs practically conform to the mesh, as confirmed by the approximately constant initial values of the condition numbers shown in Figure 13. The absence of the ghost stabilisation in Simulation (b) makes the simulation stop at the 205th time-step. This failure in the convergence of the NR is explained by the poor condition numbers exhibited by the submatrices **A** and **C** for Simulation (b), which do not permit the inversion of the Jacobian. The peak values of **A** and **C** condition numbers obtained by

Simulation (b) are approximately 19 and 15 orders of magnitude above the initial value (when the physical domain conformed to the mesh). For Simulation (a), these values are 9 and 4 orders of magnitude above the conforming value, which allows the inversion of the Jacobian throughout the analysis. In both simulations, condition numbers start to increase from the conforming value when plastic deformations occur, that is, with MPs undergoing considerable displacement from their original position, triggering the small-cut issue. It can also be noticed from Figure 13 that this mechanism occurs later in Simulation (a). This is due to the higher number of pressure degrees of freedom for Simulation (b), which permits a faster consolidation, where the total load is progressively more distributed to the effective part of the stress. The delay of plastic deformations in Simulation (a) is confirmed by Figures 15a and 15b. These contours are taken at the same time-step but show a more extensive portion of volumetric plastic strain in the case of Simulation (b).

As for the beneficial role played by Qk$_{SD}$-Qk elements, this can be appreciated in Figure 14, which reports the normalised pressure for different time steps in the row of MPs closest to the z-axis (i.e., $x = 0$, $y = 0$). In particular, Figure 14a shows how the pressure is highly oscillating in the case of Simulation (b), while Simulation
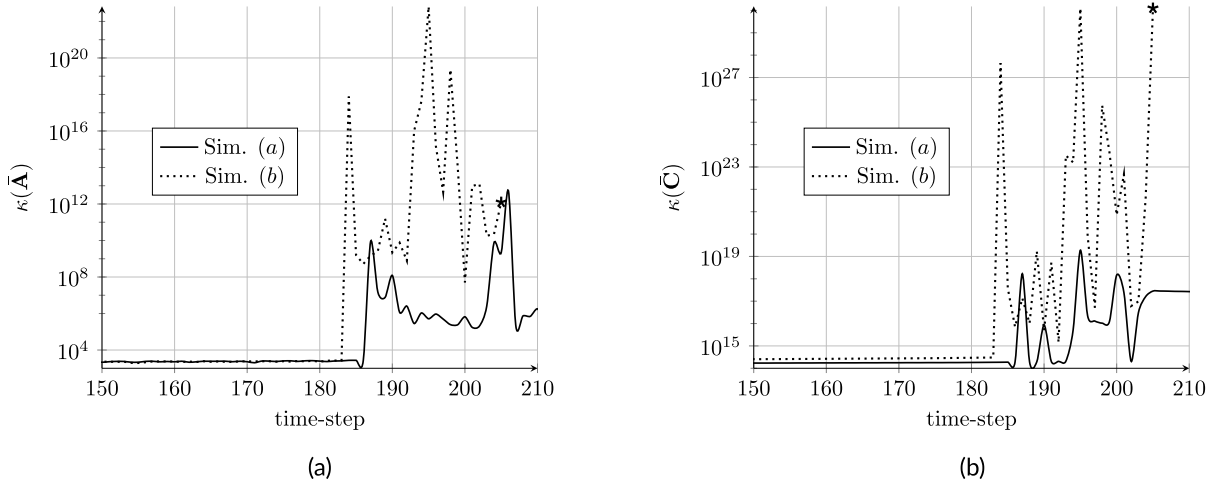
FIGURE 13 | Comparisons of the mean condition numbers of submatrices **A** (left) and **C** (right) for simulations (*a*) and (*b*), from the 150th to the 210th time step. r is defined as the counter of the NR iterations for each time-step, with N^r being its total value. Asterisks mark the final time step of simulation (*b*), where the NR algorithm fails to converge. (a) Mean condition numbers for the **A** sub-matrix for translating domains, $\kappa(\overline{\mathbf{A}}) = \frac{1}{N^r}\sum_{r=1}^{N^r}\kappa(\mathbf{A})$. (b) Mean condition numbers for the **C** sub-matrix for translating domains, $\kappa(\overline{\mathbf{C}}) = \frac{1}{N^r}\sum_{r=1}^{N^r}\kappa(\mathbf{C})$.
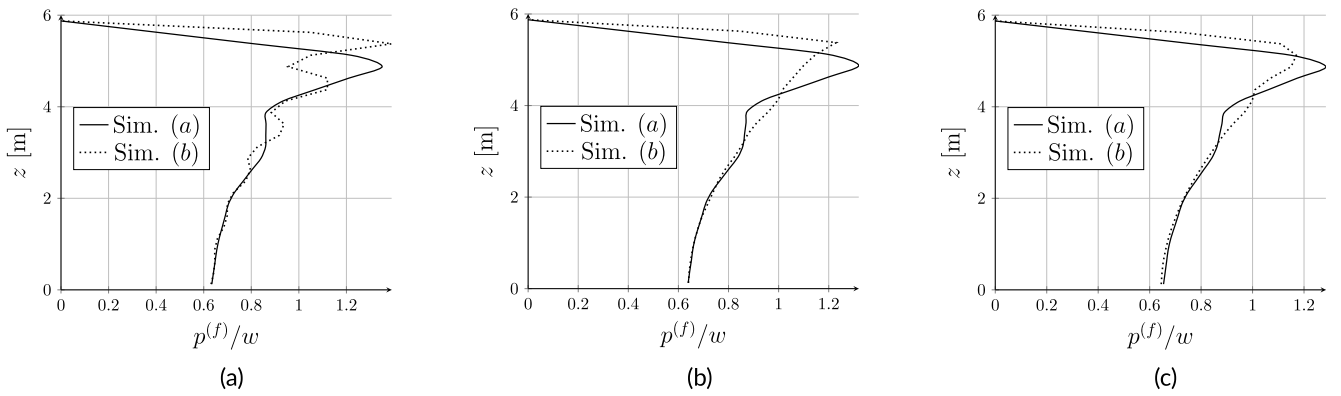

FIGURE 14 | Normalised pressures at the MPs located closest to the *z*-axis plotted along the depth of the cube. (a) Plot taken at the 1st time-step, $t \approx 0.12$ s. (b) Plot taken at the 5th time-step, $t \approx 0.63$ s. (c) Plot taken at the 10th time-step, $t \approx 1.34$ s.

(*a*) is able to represent the peak of the pressure at the top of the column without instabilities. In the case of Simulation (*b*), these instabilities are progressively removed from the simulation with time, when conditions become progressively more drained (see Figures 14b and 14c). While these instabilities seem to be entirely removed in Figure 14c, the contours of pressure in Figure 15d show that these are not entirely removed in some parts of the domain, even more towards the end of the simulation. This is not the case of Figure 15c for Simulation (*a*), where the pressure field appears smooth due to the Qk_{SD}-Qk discretisation.

6 | Conclusions

This manuscript has highlighted two sources of instability that can arise for the MPM in the case of mixed formulations and proposed a new approach that overcomes both issues for coupled (solid-fluid) problems. The intrinsic nature of the MPM as

an unfitted method and its resulting small-cut issue can lead to ill-conditioned matrices. For mixed formulations, this small-cut issue affects both the submatrices appearing on the main diagonal of the Jacobian (i.e., **A** and **C**), especially in drained conditions. The treatment of this instability has been the use of the face ghost penalty method on both the displacement and fluid pressure meshes, which, even though it does not guarantee coercivity for the MPM, limits the condition number of these submatrices (see Examples 5.2 and 5.4), thus permitting the inversion of the Jacobian matrix.

Furthermore, in nearly undrained conditions, the choices of the spaces of test and trial functions relative to displacement and pressure can violate the inf-sup condition. This work has adapted the use of Qk_{SD}-Qk elements to the MPM. The resulting overlapping meshes, while maintaining low-order shape functions (as is the case with the sMPM and the GIMPM), are stable by design (see Examples 5.3 and 5.4). This is in contrast to the widely
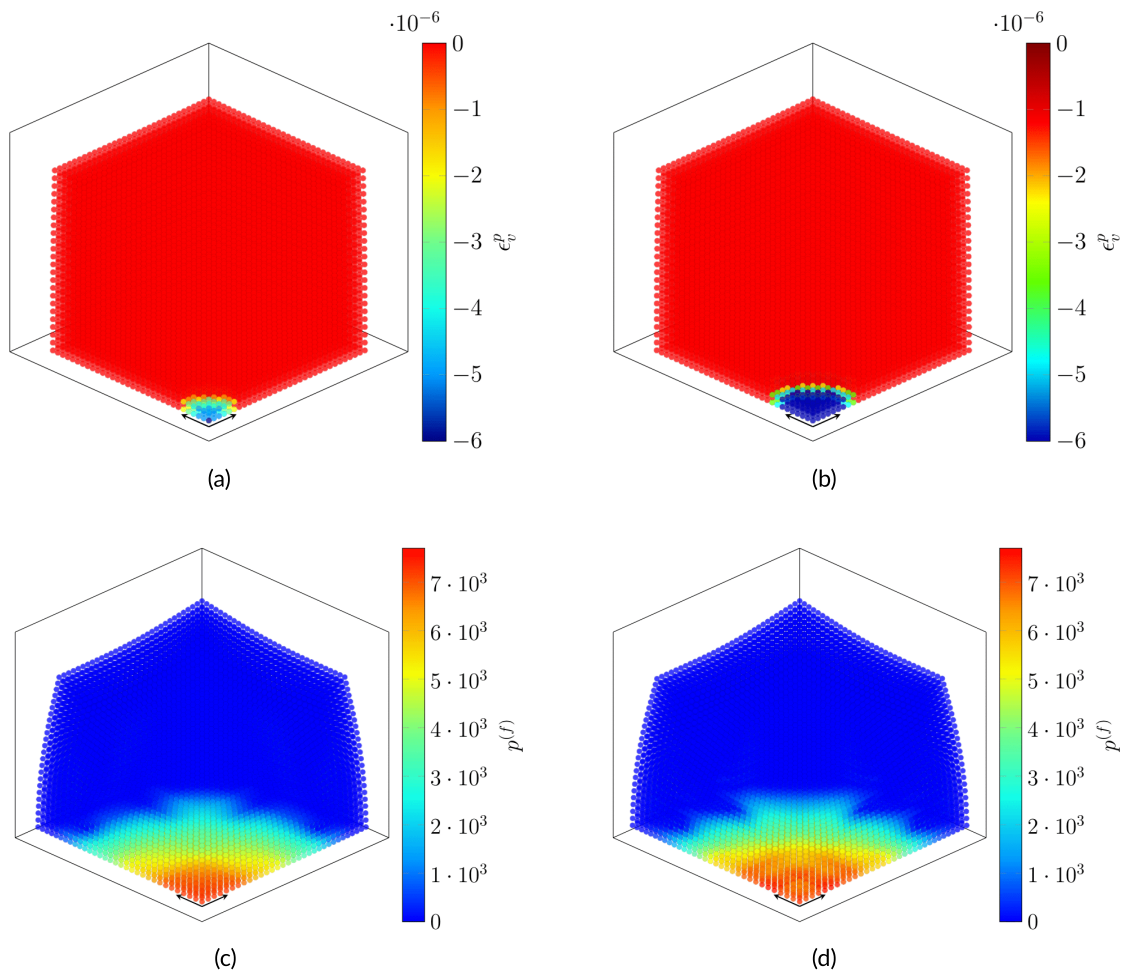
FIGURE 15 | Contours of different quantities for Simulation (*a*) (left) and (*b*) (right). These contours are computed at the 183rd time-step (top row), $t \approx 350$ s, and at the last time-step of Simulation (*b*) (bottom row), $t \approx 572$ s. (a) Contours of the volumetric plastic strain for Simulation (*a*), 183rd time-step. (b) Contours of the volumetric plastic strain for Simulation (*b*), 183rd time-step. (c) Contours of the fluid pressure for Simulation (*a*), 204th time-step. (d) Contours of the fluid pressure for Simulation (*b*), 204th time-step.

adopted PPP formulation (see Example 5.1), which is unable to stabilise poromechanical problems, especially near drained boundaries, due to the $H^1(\omega)$ nature of the pressure field [29].

The key contribution offered by this paper is a stable, implicit MPM formulation for large deformation coupled problems, including elasto-plastic material behaviour in two and three dimensions. While a rigorous analysis or even the patch test are not available for the MPM, the rationales provided throughout the paper are substantiated via the similarities between the MPM and the unfitted FEM and tested with the considered numerical examples.

Data Availability Statement

All data created during this research are openly available at http://doi.org/10.15128/r15q47rn80d.

Endnotes

[1] For the sake of completeness, a second Jacobian relative to the fluid phase could be introduced, this being given by $J^{(f)} = \det \mathbf{F}^{(f)}$, with $F_{iI}^{(f)} = \partial \varphi_i^{(f)}/\partial X_I^{(f)}$. However, since the mixture theory assumes that the current position and mixed volume are shared by the two phase particles, that is, $\mathbf{x} = \varphi^{(s)}(\mathbf{X}^{(s)}, t) = \varphi^{(f)}(\mathbf{X}^{(f)}, t)$ and $J = J^{(f)}$, the fluid deformation gradient becomes mostly redundant.

[2] Equation (14) assumes the continuum mechanics sign convention (positive pressure indicates tensile behaviour) as opposed to the geotechnical one (positive pressure designates compressive behaviour).

[3] For the fluid mass conservation, it must be noted that, technically, the correct integration domain is the fluid. However, this domain and that of the mixture are related by the Eulerian porosity, that is, $d\omega^{(f)} = n \, d\omega$. If this (i.e., the porosity) is simplified for all the terms in the fluid mass conservation, the integration over the mixture volume is *de facto* achieved.

[4] Following the convention used so far, in which vectors are in bold characters while scalars are in italics, the submatrix **C** appearing in Equation (33) should be only in italics. However, since this manuscript

makes no distinction in the notation between the continuum submatrices and their discrete counterparts, a bold font for the submatrix $\mathbf{C}$ is adopted in every context. Moreover, this makes the submatrix $\mathbf{C}$ comply with the others appearing in the Jacobian.

[5] This work often refers to the closure of a generic entity, which is a shorthand for indicating the set of entities contained by the considered generic one and the entity itself. If, for instance, a bi-dimensional mesh element T is considered, the closure of T includes the faces and nodes belonging to T and T itself.

[6] While the *face* ghost penalty is the term usually adopted in the literature, this work refers to *facet* to indicate, in the $n^{\dim}$-th dimensional space, the face with dimension $n^{\dim} - 1$, that is, a point, an edge, and a face for $n^{\dim} = 1, 2, 3$, respectively.

[7] From an implementation perspective, the current formulation can be accomplished in different ways: on the one hand, two different sets of overlapping meshes can be introduced, and the interpolant functions use the finer (in the case of displacement) or coarser (in the case of pressure) grid nodes; on the other, a unique finer mesh can be adopted, provided that the pressure interpolant functions use one node every two in each direction.

[8] This assumption can be regarded as valid if the face ghost penalty is regarded as a numerical artifice for numerical purposes (see, in this regards, Coombs [30]).

References

1. D. Sulsky, Z. Chen, and H. Schreyer, "A Particle Method for History-Dependent Materials," *Computer Methods in Applied Mechanics and Engineering* 118, no. 1-2 (1994): 179–196.

2. D. Sulsky, S. J. Zhou, and H. L. Schreyer, "Application of a Particle-in-Cell Method to Solid Mechanics," *Computer Physics Communications* 87, no. 1-2 (1995): 236–252.

3. J. Gaume, A. van Herwijnen, T. Gast, J. Teran, and C. Jiang, "Investigating the Release and Flow of Snow Avalanches at the Slope-Scale Using a Unified Model Based on the Material Point Method," *Cold Regions Science and Technology* 168 (2019): 102847.

4. J. Gaume and A. M. Puzrin, "Mechanisms of Slab Avalanche Release and Impact in the Dyatlov Pass Incident in 1959," *Communications Earth & Environment* 2, no. 1 (2021): 10.

5. D. Sulsky, H. Schreyer, K. Peterson, R. Kwok, and M. Coon, "Using the Material-Point Method to Model Sea Ice Dynamics," *Journal of Geophysical Research: Oceans* 112, no. C2 (2007).

6. A. Huth, R. Duddu, and B. Smith, "A Generalized Interpolation Material Point Method for Shallow Ice Shelves. 1: Shallow Shelf Approximation and Ice Thickness Evolution," *Journal of Advances in Modeling Earth Systems* 13, no. 8 (2021): e2020MS002277.

7. M. Xie, P. Navas, and S. Lopez-Querol, "A Stabilised Semi-Implicit Double-Point Material Point Method for Soil-Water Coupled Problems," 2024. arXiv preprint arXiv:240111951.

8. N. D. Gavin, G. Pretti, W. M. Coombs, J. C. Brigham, and C. E. Augarde, "On the Implementation of a Material Point-Based Arc-Length Method," *International Journal for Numerical Methods in Engineering* 125, no. 9 (2024): e7438.

9. J. Davy, P. Lloyd, J. H. Chandler, and P. Valdastri, "A Framework for Simulation of Magnetic Soft Robots using the Material Point Method," *IEEE Robotics and Automation Letters* (2023): 3470-3477.

10. M. Li, Y. Lei, D. Gao, Y. Hu, and X. Zhang, "A Novel Material Point Method (MPM) Based Needle-Tissue Interaction Model," *Computer Methods in Biomechanics and Biomedical Engineering* 24, no. 12 (2021): 1393–1407.

11. A. Stomakhin, C. Schroeder, L. Chai, J. Teran, and A. Selle, "A Material Point Method for Snow Simulation," *ACM Transactions on Graphics (TOG)* 32, no. 4 (2013): 1–10.

12. J. Chen, V. Kala, A. Marquez-Razon, E. Gueidon, D. A. Hyde, and J. Teran, "A Momentum-Conserving Implicit Material Point Method for Surface Tension With Contact Angles and Spatial Gradients," *ACM Transactions on Graphics (TOG)* 40, no. 4 (2021): 1–16.

13. O. Coussy, *Poromechanics* (Chichester, UK: John Wiley & Sons, 2004).

14. X. Zheng, S. Wang, F. Yang, and J. Yang, "Material Point Method Simulation of Hydro-Mechanical Behaviour in Two-Phase Porous Geomaterials: A State-of-the-Art Review". Journal of Rock Mechanics and Geotechnical," *Engineering* 16, no. 6 (2024): 2341–2350.

15. F. Ceccato, A. Yerro, and G. Di Carluccio, "Simulating Landslides With the Material Point Method: Best Practices, Potentialities, and Challenges," *Engineering Geology* 338 (2024): 107614.

16. K. Soga, E. Alonso, A. Yerro, K. Kumar, and S. Bandara, "Trends in Large-Deformation Analysis of Landslide Mass Movements With Particular Emphasis on the Material Point Method," *Géotechnique* 66, no. 3 (2016): 248–273.

17. H. A. Nøst, *Iteratively Coupled Implicit Dynamic MPM-FVM*. PhD thesis (Trondheim, Norway: Norwegian University of Science and Technology, 2019).

18. X. Zheng, *Stabilised Material Point Method for Fluid-Saturated Geomaterials*. PhD thesis (Enschede, The Netherlands: Delft University of Technology, 2022).

19. G. Pretti, *Continuum Mechanics and Implicit Material Point Method to Underpin the Modelling of Drag Anchors for Cable Risk Assessment*. PhD thesis (Durham, UK: Durham University, 2024).

20. H. Zhang, K. Wang, and Z. Chen, "Material Point Method for Dynamic Analysis of Saturated Porous Media Under External Contact/Impact of Solid Bodies," *Computer Methods in Applied Mechanics and Engineering* 198, no. 17-20 (2009): 1456–1472.

21. S. Bandara and K. Soga, "Coupling of Soil Deformation and Pore Fluid Flow Using Material Point Method," *Computers and Geotechnics* 63 (2015): 199–214.

22. Y. Zhao and J. Choo, "Stabilized Material Point Methods for Coupled Large Deformation and Fluid Flow in Porous Materials," *Computer Methods in Applied Mechanics and Engineering* 362 (2020): 112742.

23. S. Kularathna, W. Liang, T. Zhao, B. Chandra, J. Zhao, and K. Soga, "A Semi-Implicit Material Point Method Based on Fractional-Step Method for Saturated Soil," *International Journal for Numerical and Analytical Methods in Geomechanics* 45, no. 10 (2021): 1405–1436.

24. J. Yu, J. Zhao, W. Liang, and S. Zhao, "A Semi-Implicit Material Point Method for Coupled Thermo-Hydro-Mechanical Simulation of Saturated Porous Media in Large Deformation," *Computer Methods in Applied Mechanics and Engineering* 418 (2024): 116462.

25. J. Yu, J. Zhao, S. Zhao, and W. Liang, "Thermo-Hydro-Mechanical Coupled Material Point Method for Modeling Freezing and Thawing of Porous Media," *International Journal for Numerical and Analytical Methods in Geomechanics* 48 (2024): 3308–3349.

26. S. Hidano, Y. Yamaguchi, S. Takase, S. Moriguchi, K. Kaneko, and K. Terada, "Semi-Implicit Material Point Method for Simulating Infiltration-Induced Failure of Unsaturated Soil Structures," *International Journal for Numerical and Analytical Methods in Geomechanics* 48, no. 10 (2024): 2661–2699.

27. C. Taylor and P. Hood, "A Numerical Solution of the Navier-Stokes Equations Using the Finite Element Technique," *Computers & Fluids* 1, no. 1 (1973): 73–100.

28. X. Zheng, F. Pisanò, P. J. Vardon, and M. A. Hicks, "An Explicit Stabilised Material Point Method for Coupled Hydromechanical Problems

in Two-Phase Porous Media," *Computers and Geotechnics* 135 (2021): 104112.

29. M. Preisig and J. H. Prévost, "Stabilization Procedures in Coupled Poromechanics Problems: A Critical Assessment," *International Journal for Numerical and Analytical Methods in Geomechanics* 35, no. 11 (2011): 1207–1225.

30. W. M. Coombs, "Ghost Stabilisation of the Material Point Method for Stable Quasi-Static and Dynamic Analysis of Large Deformation Problems," *International Journal for Numerical Methods in Engineering* 124, no. 21 (2023): 4841–4875.

31. E. Burman and P. Hansbo, "Fictitious Domain Methods Using Cut Elements: III. A Stabilized Nitsche Method for Stokes' Problem," *ESAIM: Mathematical Modelling and Numerical Analysis-Modélisation Mathématique et Analyse Numérique* 48, no. 3 (2014): 859–874.

32. S. G. Bardenhagen and E. M. Kober, "The Generalized Interpolation Material Point Method," *Computer Modeling in Engineering and Sciences* 5, no. 6 (2004): 477–496.

33. T. Charlton, W. Coombs, and C. Augarde, "IGIMP: An Implicit Generalised Interpolation Material Point Method for Large Deformations," *Computers & Structures* 190 (2017): 108–125.

34. V. P. Nguyen, A. de Vaucorbeil, and S. Bordas, *The Material Point Method: Theory* (Springer Nature: Implementations and Applications, 2023).

35. J. E. Guilkey and J. A. Weiss, "Implicit Time Integration for the Material Point Method: Quantitative and Algorithmic Comparisons With the Finite Element Method," *International Journal for Numerical Methods in Engineering* 57, no. 9 (2003): 1323–1338.

36. W. M. Coombs, C. E. Augarde, A. J. Brennan, et al., "On Lagrangian Mechanics and the Implicit Material Point Method for LARGE Deformation Elasto-Plasticity," *Computer Methods in Applied Mechanics and Engineering* 358 (2020): 112622.

37. E. Kröner, "Allgemeine Kontinuumstheorie der Versetzungen und Eigenspannungen," *Archive for Rational Mechanics and Analysis* 4, no. 1 (1959): 273–334.

38. E. H. Lee, "Elastic-Plastic Deformation at Finite Strains," *Journal of Applied Mechanics* 36, no. 1 (1969): 1–6.

39. J. Mandel, "Plasticité Classique et Viscoplasticité," in *of CISM Courses and Lectures*, vol. 97 (New York, NY: Springer, 1971).

40. J. F. Thorpe, "On the Momentum Theorem for a Continuous System of Variable Mass," *American Journal of Physics* 30, no. 9 (1962): 637–640.

41. R. I. Borja and E. Alarcón, "A Mathematical Framework for Finite Strain Elastoplastic Consolidation Part 1: Balance Laws, Variational Formulation, and Linearization," *Computer Methods in Applied Mechanics and Engineering* 122, no. 1-2 (1995): 145–171.

42. G. Pretti, W. M. Coombs, C. E. Augarde, M. M. Puigvert, and J. A. R. Gutiérrez, "Preserving Non-Negative Porosity Values in a Bi-Phase Elasto-Plastic Material Under Terzaghi's Effective Stress Principle," *Mechanics of Materials* 192 (2024): 104958.

43. C. Miehe, S. Mauthe, and S. Teichtmeister, "Minimization Principles for the Coupled Problem of Darcy–Biot-Type Fluid Transport in Porous Media Linked to Phase Field Modeling of Fracture," *Journal of the Mechanics and Physics of Solids* 82 (2015): 186–217.

44. B. Dortdivanlioglu, A. Krischok, L. Beirão da Veiga, and C. Linder, "Mixed Isogeometric Analysis of Strongly Coupled Diffusion in Porous Materials," *International Journal for Numerical Methods in Engineering* 114, no. 1 (2018): 28–46.

45. D. Boffi, F. Brezzi, M. Fortin, et al., *Mixed Finite Element Methods and Applications*, vol. 44 (Heidelberg, Germany: Springer, 2013).

46. P. Mira, M. Pastor, T. Li, and X. Liu, "A New Stabilized Enhanced Strain Element With Equal Order of Interpolation for Soil Consolidation

Problems," *Computer Methods in Applied Mechanics and Engineering* 192, no. 37-38 (2003): 4257–4277.

47. D. Chapelle and K. J. Bathe, "The inf-sup Test," *Computers & Structures* 47, no. 4-5 (1993): 537–545.

48. B. Nedjar, "Formulation of a Nonlinear Porosity Law for Fully Saturated Porous Media at Finite Strains," *Journal of the Mechanics and Physics of Solids* 61, no. 2 (2013): 537–556.

49. B. Nedjar, "On Finite Strain Poroplasticity With Reversible and Irreversible Porosity Laws. Formulation and Computational Aspects," *Mechanics of Materials* 68 (2014): 237–252.

50. R. Bird, G. Pretti, W. Coombs, et al., "An Implicit Material Point-to-Rigid Body Contact Approach for Large Deformation Soil-Structure Interaction," *Computers and Geotechnics* 174 (2024): 106646.

51. E. Burman, "Ghost Penalty," *Comptes Rendus Mathematique* 348, no. 21-22 (2010): 1217–1220.

52. E. Burman, P. Hansbo, and M. G. Larson, "On the Design of Locking Free Ghost Penalty Stabilization and the Relation to CutFEM With Discrete Extension," 2022. arXiv preprint arXiv:220501340.

53. Z. Liu, Y. Zhang, Y. Jiang, H. Yang, and Y. Yang, "Unfitted Finite Element Method for Fully Coupled Poroelasticity With Stabilization," *Computer Methods in Applied Mechanics and Engineering* 397 (2022): 115132.

54. Y. Yamaguchi, S. Moriguchi, and K. Terada, "Extended B-spline-Based Implicit Material Point Method," *International Journal for Numerical Methods in Engineering* 122, no. 7 (2021): 1746–1769.

55. K. Höllig, U. Reif, and J. Wipper, "Weighted Extended B-Spline Approximation of Dirichlet Problems," *SIAM Journal on Numerical Analysis* 39, no. 2 (2001): 442–462.

56. K. Höllig, *Finite Element Methods With B-splines* (Philadelphia, PA: SIAM, 2003).

57. S. Badia, F. Verdugo, and A. F. Martín, "The Aggregated Unfitted Finite Element Method for Elliptic Problems," *Computer Methods in Applied Mechanics and Engineering* 336 (2018): 533–553.

58. M. Bercovier and O. Pironneau, "Error Estimates for Finite Element Method Solution of the Stokes Problem in the Primitive Variables," *Numerische Mathematik* 33 (1979): 211–224.

59. A. A. Madadi and B. Dortdivanlioglu, "A Subdivision-Stabilized B-spline Mixed Material Point Method," *Computer Methods in Applied Mechanics and Engineering* 418 (2024): 116567.

60. G. Leborgne, "Inf-sup Condition and Locking: Understanding and Circumventing," *Stokes, Laplacian, bi-Laplacian, Kirchhoff–Love and Mindlin–Reissner Locking Type, Boundary Conditions.* arXiv preprint arXiv:230104373 (2023). https://doi.org/10.48550/arXiv.2301.04373

61. W. Sun, J. T. Ostien, and A. G. Salinger, "A Stabilized Assumed Deformation Gradient Finite Element Formulation for Strongly Coupled Poromechanical Simulations at Finite Strain," *International Journal for Numerical and Analytical Methods in Geomechanics* 37, no. 16 (2013): 2755–2788.

62. E. Love and D. L. Sulsky, "An Unconditionally Stable, Energy–Momentum Consistent Implementation of the Material-Point Method," *Computer Methods in Applied Mechanics and Engineering* 195, no. 33-36 (2006): 3903–3925.

63. G. Pretti, W. M. Coombs, C. E. Augarde, B. Sims, M. M. Puigvert, and J. A. R. Gutiérrez, "A Conservation Law Consistent Updated Lagrangian Material Point Method for Dynamic Analysis," *Journal of Computational Physics* 485 (2023): 112075.

64. W. M. Coombs and C. E. Augarde, "AMPLE: A Material Point Learning Environment," *Advances in Engineering Software* 139 (2020): 102748.

65. K. Terzaghi, *Theoretical Soil Mechanics* (New York: John Wiley & Sons, 1943).

66. J. A. White and R. I. Borja, "Stabilized Low-Order Finite Elements for Coupled Solid-Deformation/Fluid-Diffusion and Their Application to Fault Zone Transients," *Computer Methods in Applied Mechanics and Engineering* 197, no. 49-50 (2008): 4353–4366.

67. P. Vermeer and A. Verruijt, "An Accuracy Condition for Consolidation by Finite Elements," *International Journal for Numerical and Analytical Methods in Geomechanics* 5, no. 1 (1981): 1–14.

68. L. Monforte, P. Navas, J. M. Carbonell, M. Arroyo, and A. Gens, "Low-Order Stabilized Finite Element for the Full Biot Formulation in Soil Mechanics at Finite Strain," *International Journal for Numerical and Analytical Methods in Geomechanics* 43, no. 7 (2019): 1488–1515.

69. C. R. Dohrmann and P. B. Bochev, "A Stabilized Finite Element Method for the Stokes Problem Based on Polynomial Pressure Projections," *International Journal for Numerical Methods in Fluids* 46, no. 2 (2004): 183–201.

70. S. Badia, E. Neiva, and F. Verdugo, "Linking Ghost Penalty and Aggregated Unfitted Methods," *Computer Methods in Applied Mechanics and Engineering* 388 (2022): 114232.

71. H. Kothari and R. Krause, "A Generalized Multigrid Method for Solving Contact Problems in Lagrange Multiplier Based Unfitted Finite Element Method," *Computer Methods in Applied Mechanics and Engineering* 392 (2022): 114630.

72. S. Sticko, G. Ludvigsson, and G. Kreiss, "High-Order Cut Finite Elements for the Elastic Wave Equation," *Advances in Computational Mathematics* 46, no. 3 (2020): 1–28.

73. F. Armero, "Formulation and Finite Element Implementation of a Multiplicative Model of Coupled Poro-Plasticity at finite strains under fully saturated conditions," *Computer Methods in Applied Mechanics and Engineering* 171, no. 3-4 (1999): 205–241.

74. I. F. Collins and T. Hilder, "A Theoretical Framework for Constructing Elastic/Plastic Constitutive Models of Triaxial Tests," *International Journal for Numerical and Analytical Methods in Geomechanics* 26, no. 13 (2002): 1313–1347.

75. W. M. Coombs and R. S. Crouch, "Algorithmic Issues for Three-Invariant Hyperplastic Critical State Models," *Computer Methods in Applied Mechanics and Engineering* 200, no. 25-28 (2011): 2297–2318.

76. C. Miehe, "Comparison of Two Algorithms for the Computation of Fourth-Order Isotropic Tensor Functions," *Computers & Structures* 66, no. 1 (1998): 37–43.

Appendix A

Linearisation of the Adopted Finite Strain Formulation

This section reports the Jacobian matrix resulting from the linearisation of stable Equations (47) and (48). For brevity and clarity of notation, the subscript indicating the current $n + 1$ time-step is omitted. Equations (47) and (48) are repeated below, with the assumption that the matrices relative to the ghost penalties are computed at the previously converged step (n-th time-step)[8], that is,

$$
\delta \mathbf{w}_a \left(\underbrace{\int_{MP_\omega} \mathbf{grad}(N_a^{h/2}) : \boldsymbol{\sigma}' \, dv}_{:=\mathbf{f}_a'^{\text{int}}} - \underbrace{\int_{MP_\omega} \mathbf{grad}(N_a^{h/2}) N_b^h : \mathbf{1} \, dv}_{:=\mathbf{K}_{ab}^{(f)\,\text{int}}} \mathrm{p}_b \right.
$$
$$
- \underbrace{\left(\int_{MP_\omega} N_a^{h/2} \cdot \rho \boldsymbol{b} \, dv + \int_{\gamma^{\bar{t}}} N_a^{h/2} \cdot \bar{\boldsymbol{t}} \, da \right)}_{:=\mathbf{f}_a^{\text{ext}}}
$$
$$
\left. + \underbrace{\gamma^A \frac{h}{2} \int_{h/2_{\gamma}F} [[(\mathbf{grad}_n(N_a^{h/2}) \cdot \mathbf{n}_n)]] \cdot [[(\mathbf{grad}_n(N_b^{h/2}) \cdot \mathbf{n}_n)]] \, da_n}_{:=\mathbf{K}_{ab}^{\text{ghst}}} \mathbf{u}_b \right) = 0,
$$
$$
\forall \delta \mathbf{w}_a \in {}^{h/2}\mathcal{V}_0 \tag{A1}
$$

$$
\delta \eta_a \left(\underbrace{\int_{MP_\omega} N_a^h \, \rho_0^{(f)} \frac{(\ln J - \ln J_n)}{\Delta t} \, dv}_{:=\mathrm{v}_a^{\text{int}}} + \underbrace{\int_{MP_\omega} \frac{\kappa}{g} \, \mathbf{grad}(N_a^h) \cdot \mathbf{grad}(N_b^h) dv}_{:=\mathrm{Q}_{ab}^{\text{press}}} \mathrm{p}_b \right.
$$
$$
+ \underbrace{\gamma^{\text{pen}} \int_{\gamma^{\bar{p}}} N_a^h \, (N_b^h \, \mathrm{p}_b - \bar{p}) da}_{:=\mathrm{v}_a^{\text{pen}}} - \underbrace{\left(\int_{MP_\omega} \frac{\kappa}{g} \, \mathbf{grad}(N_a^h) \cdot \rho_0^{(f)} \boldsymbol{b} \, dv + \int_{\gamma^{\bar{q}}} N_a^h \, \bar{q} \, da \right)}_{:=\mathrm{v}_a^{\text{ext}}}
$$
$$
\left. + \underbrace{\gamma^C h \int_{h_{\gamma}F} [[(\mathbf{grad}_n(N_a^h) \cdot \mathbf{n}_n)]] [[(\mathbf{grad}_n(N_b^h) \cdot \mathbf{n}_n)]] \, da_n}_{:=\mathrm{Q}_{ab}^{\text{ghst}}} \mathrm{p}_b \right) = 0,
$$
$$
\forall \delta \eta_a \in {}^h\mathcal{W}_0 \tag{A2}
$$

The variation of the above equations (second variation of functionals) gives the following matrices

$$
\mathbf{A}_{ab} = \delta \left(\mathbf{f}_a'^{\text{int}} - \mathbf{K}_{ac}^{(f)\,\text{int}} \mathrm{p}_c - \mathbf{f}_a^{\text{ext}} + \mathbf{K}_{ac}^{\text{ghst}} \mathbf{u}_c, \delta \mathbf{u}_b \right) \tag{A3}
$$

$$
\mathbf{B}_{ab}^{(1)} = \delta \left(-\mathbf{K}_{ac}^{(f)\,\text{int}} \, \mathrm{p}_c, \delta \mathrm{p}_b \right) \tag{A4}
$$

$$
\mathbf{B}_{ab}^{(2)} = \delta \left(\mathrm{v}_a^{\text{int}} + \mathrm{Q}_{ac}^{\text{press}} \, \mathrm{p}_c - \mathrm{v}_a^{\text{ext}}, \delta \mathbf{u}_b \right) \tag{A5}
$$

$$
\mathbf{C}_{ab} = \delta \left(\mathrm{Q}_{ac}^{\text{press}} \, \mathrm{p}_c + \mathrm{v}_a^{\text{pen}} + \mathrm{Q}_{ac}^{\text{ghst}} \, \mathrm{p}_c, \delta \mathrm{p}_b \right) \tag{A6}
$$

Let us recall the Cartesian basis vectors introduced in Section 2.1 for the current configuration $\boldsymbol{e}_i$ and for the initial one $\boldsymbol{E}_I$, which are employed to express the Cartesian components of the tensors and vectors appearing above. In particular, it follows from Equation (A3) that

$$
\delta \left(\mathbf{f}_a'^{\text{int}}, \delta \mathbf{u}_b \right) = \int_{MP_\omega} \mathrm{grad}_h \left(\mathbf{N}_{ai}^{h/2} \right) \left(-\tau'_{ik} \, \delta_{hj} + a_{\text{ihjk}} \right) \mathrm{grad}_k \left(\mathbf{N}_{bj}^{h/2} \right) dV \tag{A7}
$$

$$
\delta \left(\mathbf{K}_{ac}^{(f)\,\text{int}} \mathrm{p}_c, \delta \mathbf{u}_b \right) = \int_{MP_\omega} \mathrm{grad}_h \left(\mathbf{N}_{ai}^{h/2} \right) \left(-\delta_{ik} \, \delta_{hj} + \delta_{jk} \, \delta_{ih} \right) \mathrm{grad}_k \left(\mathbf{N}_{bj}^{h/2} \right) N_c^h \, dv \, \mathrm{p}_c \tag{A8}
$$

$$
\delta \left(\mathbf{f}_a^{\text{ext}}, \delta \mathbf{u}_b \right) = \int_{MP_\omega} \rho_0^{(f)} \mathbf{N}_{ai}^{h/2} \, b_i \, \delta_{jk} \, \mathrm{grad}_k \left(\mathbf{N}_{bj}^{h/2} \right) dv \tag{A9}
$$

$$
\delta \left(\mathbf{K}_{ac}^{\text{ghst}} \mathbf{u}_c, \delta \mathbf{u}_b \right) = \mathbf{K}_{ab}^{\text{ghst}} \tag{A10}
$$

where dV indicates the initial volume of integration, δ_{ij} is the Kronecker delta, and the fourth-order tensor a_{ihjk} depends on the considered constitutive relationship. In the case of a Hencky material, this is given by

$$
a_{\text{ihjk}} = \frac{1}{2} D_{\text{ihpq}}'^{\text{alg}} \, L_{\text{pqrs}} \, B_{\text{rsjk}} \tag{A11}
$$

where

$$
D_{\text{ihpq}}'^{\text{alg}} = \frac{\partial \tau'_{ih}}{\partial \epsilon_{pq}^{e,\,tr}}, \quad L_{\text{pqrs}} = \frac{\partial \ln b_{pq}^{e,\,tr}}{\partial b_{rs}^{e,\,tr}}, \quad B_{\text{rsjk}} = \delta_{rj} b_{ks}^{e,\,tr} + b_{rk}^{e,\,tr} \delta_{sj}. \tag{A12}
$$

The full expression of $D_{\text{ihpq}}'^{\text{alg}}$ can be found in Pretti et al. [42] for the improved Hencky material under consideration (see Equation 15), while a convenient expression for L_{pqrs} is given in Miehe [76]. The component of Equation (A4) is straightforwardly given by

$$
\delta \left(\mathbf{K}_{ac}^{(f)\,\text{int}} \, \mathrm{p}_c, \delta \mathrm{p}_b \right) = \mathbf{K}_{ab}^{(f)\,\text{int}} \tag{A13}
$$

while those of Equation (A5) are as follows

$$
\delta \left(\mathrm{v}_a^{\text{int}}, \delta \mathbf{u}_b \right) = \int_{MP_\omega} \rho_0^{(f)} N_a^h \, \frac{(1 + \ln J - \ln J_n)}{\Delta t} \delta_{kj} \, \mathrm{grad}_k \left(\mathbf{N}_{bj}^{h/2} \right) dv \tag{A14}
$$

$$\delta\left(Q_{ac}^{\text{press}}\, p_c, \delta\mathbf{u}_b\right) = \int_{MP_\omega} \frac{1}{g}\left(\left(c_1\frac{n^2(3-n)}{(1-n)^2}+\kappa\right)\text{grad}_i\left(N_a^h\right)\text{grad}_i\left(N_c^h\right)\delta_{jk}\right.$$
$$\left. - \kappa\left(\text{grad}_j\left(N_a^h\right)\text{grad}_k\left(N_c^h\right)+\text{grad}_k\left(N_a^h\right)\text{grad}_j\left(N_c^h\right)\right)\right)\text{grad}_k\left(\mathbf{N}_{bj}^{h/2}\right)dv\, p_c \quad \text{(A15)}$$

$$\delta\left(v_a^{\text{ext}}, \delta\mathbf{u}_b\right) = \int_{MP_\omega} \frac{\rho_0^{(f)}}{g}\left(\left(c_1\frac{n^2(3-n)}{(1-n)^2}+\kappa\right)\delta_{jk}\,\text{grad}_i\left(N_a^h\right)\right.$$
$$\left. - \kappa\,\delta_{ik}\,\text{grad}_j\left(N_a^h\right)\right)b_i\,\text{grad}_k\left(\mathbf{N}_{bj}^{h/2}\right)dv \quad \text{(A16)}$$

Components of Equation (A6) are finally given by

$$\delta\left(Q_{ac}^{\text{press}}\, p_c, \delta p_b\right) = Q_{ab}^{\text{press}} \quad \text{(A17)}$$

$$\delta\left(v_a^{\text{pen}}, \delta p_b\right) = \gamma^{\text{pen}}\int_{\gamma^{\bar{p}}} N_a^h\left(N_b^h\right)da \quad \text{(A18)}$$

$$\delta\left(Q_{ac}^{\text{ghst}}\, p_c, \delta p_b\right) = Q_{ab}^{\text{ghst}} \quad \text{(A19)}$$

As it can be seen from the above equations, the ghost stabilisation adds components to the submatrices **A** and **C** (see Equations A3 and A6) to guarantee the required coercivity of these matrices, as detailed in Section 3.2.